RE-486

SPECIMEN ANALYSIS OF SKYLAB, M553 EXPERIMENT, FLIGHT SPECIMENS

August 1974

RE-486

SPECIMEN ANALYSIS OF SKYLAB, M553 EXPERIMENT, FLIGHT SPECIMENS†

Final Report on Phase C
Contract NAS 8-28728

Prepared for

George C. Marshall Space Flight Center
Marshall Space Flight Center
Alabama 35812

August 1974

† This investigation was partially funded by the National Aeronautics and Space Administration under Contract NAS 8-28728

D. J. Larson, Jr.

Research Department
Materials and Structural Mechanics
Grumman Aerospace Corporation
Bethpage, New York 11714

Approved by: Charles E Mack Jr
Charles E. Mack, Jr.
Director of Research

ABSTRACT

Metallurgical analyses were conducted on six Skylab II flight samples to study containerless solidification and the effects of weightlessness on the solidification process.

Results indicate an outstanding record of solute redistribution processes and of solidification terracing; this record may exceed that obtainable terrestrially. The solute redistribution process was found to be highly localized and in some cases this localization was to prescribed, low index, crystallographic systems. Some samples demonstrated that under reduced pressure and gravity conditions the anticipated solid/liquid solidification process was perturbed and superseded by solid/liquid/gas reactions during melting and solidification.

TABLE OF CONTENTS

LIST OF ILLUSTRATIONS

INTRODUCTION

As part of its efforts in the Space Processing (SP) program, NASA conducted experiments in the Skylab program with the ultimate goal of manufacturing useful products economically in space. The M553 Sphere Forming Experiment was conducted within the M512 Furnace Facility of Skylab II to study the effects of a reduced gravity environment on solidification processes.

Six of the samples generated in these experiments were evaluated by the Grumman Research Department. This report describes the metallurgical results.

EXPERIMENTAL RESULTS AND DISCUSSION

The M553 Metals Melting and Solidification Experiment was designed to study the effects of a reduced gravity environment on the containerless solidification of four different materials. Each of these materials has a face centered cubic (fcc) primary structure, and these materials were chosen because the solidification theory is most advanced for this atomic structure (Ref. 1). The four materials selected were, nominally, pure Ni, Ni-1 wt% Ag, Ni-12 wt% Sn, and Ni-30 wt% Cu.

Although these materials were all of the fcc crystal structure, they were expected to differ in their solidification behavior because of the differing alloy contents. Pure Ni was expected to solidify in a congruent fashion whereas the alloys were expected to solidify athermally and to demonstrate constitutional supercooling. More specifically, the limited solute content of the Ni-1Ag alloy was expected to result in a cellular solidification mode over a narrow temperature range, whereas the remaining two alloys were expected to solidify dendritically over a wider temperature range. The solidification of the higher concentration alloys differed in that the Ni-30Cu alloy was a single-phase material whereas the Ni-12Sn alloy was a two-phase eutectic mixture of Ni and Ni_3Sn. The materials could be further differentiated, by solidification reaction, in that the phase pure nickel solidified congruently, the Ni-1Ag solidified via monotectic reaction, the Ni-12Sn solidified eutectically, and the Ni-30Cu solidified as an isomorphous solid solution. Clearly, the sample consisted of a group of materials representative of a wide range of solute content and of phase reactions representative of a large segment of metallurgical practice. The published (Ref. 2) phase diagrams are included as Appendix A.

The unprocessed materials were chamfered cylinders and melted by an electron beam that impinged on a sample from one side. The samples were arranged on a "pinwheel" (Fig. 1) that could be

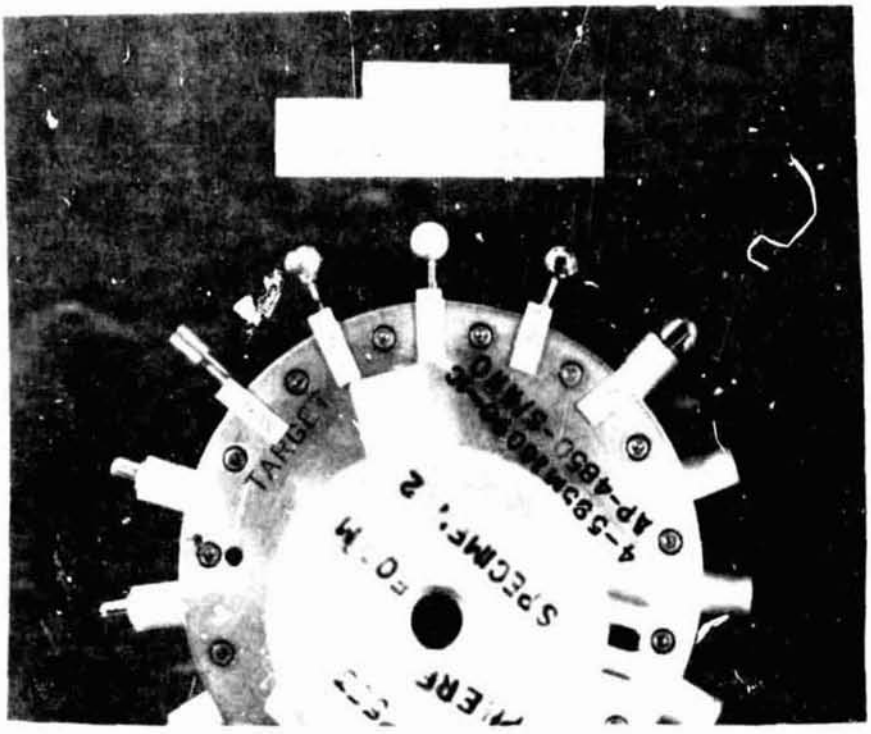

Fig. 1 Pinwheel 2 As Returned from Skylab II (1×)

rotated by an index motor such that the samples were melted sequentially. There were 15 index positions on the "pinwheel" and it should be noted that position 1 was reserved for a tungsten target for focusing the electron beam and the remaining 14 specimen positions incorporated both retained "sting" specimens (positions 2-5) and free float specimens (positions 6-15). The retained specimens are shown in Fig. 1 with some unmelted samples. The materials were arranged in a designed sequence to maximize the scientific return and this sequence is tabulated in Table 1. Each of the pinwheels processed during Skylab II had the same sequence of materials and the melting of each specimen was started at a vacuum of

TABLE 1 MATERIALS SEQUENCE FOR M553 SPECIMEN "PINWHEELS"

Index No.	Specimen Materials	Process Type
1	Tungsten	Target
2	Ni	Retained
3	Ni-12Sn	Retained
4	Ni-1Ag	Retained
5	Ni	Free Float
6	Ni	Free Float
7	Ni-12Sn	Free Float
8	Ni-1Ag	Free Float
9	Ni-30Cu	Free Float
10	Ni-30Cu	Free Float
11	Ni-1Ag	Free Float
12	Ni-12Sn	Free Float
13	Ni	Free Float
14	Ni-12Sn	Free Float
15	Ni-1Ag	Free Float

Note: The index number is preceded by the specimen pinwheel number in identifying samples, and the specimen pinwheels both used the same specimen material sequence.

10^{-5} mm Hg. Unfortunately, the released specimens could not be singularly identified and so not all of the sample numbers used to identify distributed samples correspond with the original specimen pinwheel index numbers. Note (in subsequent sections) that some samples intended to be released from their pedestals while molten, did not, and others, although released, impacted on chamber surfaces while still molten. The latter are not strictly representative of materials solidified while floating freely in a reduced gravity environment.

This report considers each alloy; however, distinctive features of each sample are identified individually. Where possible, generalizations are drawn covering all samples and results are compared with the as-received materials (Ref. 3) and samples processed in a one-gravity field (Ref. 4). Samples of the same nominal chemistry are considered in sequence for the sake of continuity. The physical and mechanical properties of the as-received and ground-base samples are included in Tables 2-5 and are incorporated in the individual flight sample discussions.

Sample 1-15

This was a partially melted, pure nickel, sample that released prematurely and impacted, while partially molten, within the furnace chamber. The sample is shown in orthogonal views macroscopically in Figs. 2a and 2b. The lower portion of Fig. 2a clearly shows the extent of the remnant unmelted solid and the flattened upper portion resulted from the impact of the molten portion within the chamber.

Figure 3 is an enlargement of one of the shrinkage cavities on the impact surface shown in Fig. 2b. The most interesting aspect of this is that the solidification morphology appears cellular. This is impossible for a phase pure material and indicates that the sample, or at least this portion of the sample, is contaminated. Consideration of the surface contamination levels of this sample, as shown in Table 6, indicates that substantial levels of aluminum, copper, and silver contamination are present on all of the sample surfaces. However, there is an increased aluminum contamination level that progresses from the top of the sample toward the base of the sample. This would indicate that the aluminum contamination emanated from the Al_2O_3 pedestal and the aluminum content increases with proximity to the pedestal area.

TABLE 2 AS-RECEIVED PROPERTIES OF MATERIALS USED IN THIS STUDY

Sample No.	Nominal Comp (Wt%)	Descriptor (Microstructure)	Hardness DPH	Curie Pt °C	Liquidus, °C	Solidus, °C	T_{mean} °C
1	Ni	Wrought	275	358	1462	1446	1454
		Annealed	90				
2	Ni-1Ag	As-Cast	72	351	1475	1405	1440
3	Ni-12Sn	Annealed	290	105	1373	1268	1320
4	Ni-30Cu	Annealed	160	58	1350	1310	1330

TABLE 3 CALCULATED AND EXPERIMENTAL LATTICE PARAMETERS

Sample No.	Nominal Comp (Wt %)	a_o^{th}	$a_{o_{exp}}$
1	Ni	3.5355	3.534 ± 0.001
2	Ni-1Ag	3.5385	3.533 ± 0.001
3	Ni-12Sn	3.5945	3.593 ± 0.005
4	Ni-30Cu	3.5625	3.5325 ± 0.0006 (B-3)

† Theoretical values were calculated utilizing the assumption of ideal mixing with no electronegative interaction and Goldschmidt radii of 1.25, 1.28, 1.44, and 1.58 for Ni, Cu, Ag, and Sn, respectively. These values have been corrected to twelvefold coordination in each case.

TABLE 4 PHYSICAL AND MECHANICAL PROPERTY MEASUREMENTS GROUND-BASE SAMPLES (Ref. 2)

Sample No.	Comp (Wt %)	Wt gm	Region	Grain Size mm	Descriptor	Hardness, DPH	Curie Pt °C	Sphericity (R_{max}/R_{min})
1-6	Ni	1.2752	Surface	1.00	Equiaxed Dendrites	70	358	1.28
			Interior	1.00	Equiaxed			
1-10	Ni-30Cu	1.1933	Surface	0.10	Equiaxed Dendrites, "Cap"			
			Interior	0.20	Equiaxed Dendrites, "Cap"			
			Interior	0.8 x 0.2	Columnar Dendrites	85	Not Measured	1.29
1-15	Ni-1Ag	1.1855	Surface	0.2	Equiaxed Dendrites, "Cap"			
			Interior	0.5 x 1.0	Equiaxed Dendrites, "Cap"			
			Interior	0.5 x 2.0	Columnar Dendrites	58	Not Measured	1.34
2-3	Ni-12Sn	1.2000	Surface	0.15	Equiaxed Dendrites, "Cap"			
			Interior	0.15	Equiaxed Dendrites, "Cap"	185	Not Measured	1.29
2-12	Ni-12Sn	1.1700	Surface	0.14	Equiaxed Dendrites, "Cap"			
			Interior	0.15	Equiaxed Dendrites. 'Cap"	185	Not Measured	1.50

TABLE 5 LATTICE PARAMETER MEASUREMENTS

Sample No.	Comp	a_o^{th}	a^{ADJ}	$\bar{a}_o$	$a_{o_{exp}}$	Description
1-6	Pure Ni	3.5355	3.5238	3.5208	3.5208	Equiaxed Grains (Internal)
1-10	Ni-30Cu	3.5625	3.5507	3.5554		Interior
					3.5415	Surface, Solute Rich (Cap)
					3.5242	Surface, Solute Poor (Cap)
					3.5575	Surface, Solute Rich (Dendrites)
					3.5287	Surface, Solute Poor (Dendrites)
1-15	Ni-1Ag	3.5385	3.5268	3.5280	3.5278	Interior
2-12	Ni-12Sn	3.5945	3.5826	3.5781		Surface
					3.6082	Surface, Solute Rich
					3.5490	Surface, Solute Poor
				3.5815		Interior
2-3	Ni-12Sn	3.5945	3.5826	3.5830		Surface
					3.6112	Surface, Solute Rich
					3.5547	Surface, Solute Poor
				3.5846		Interior

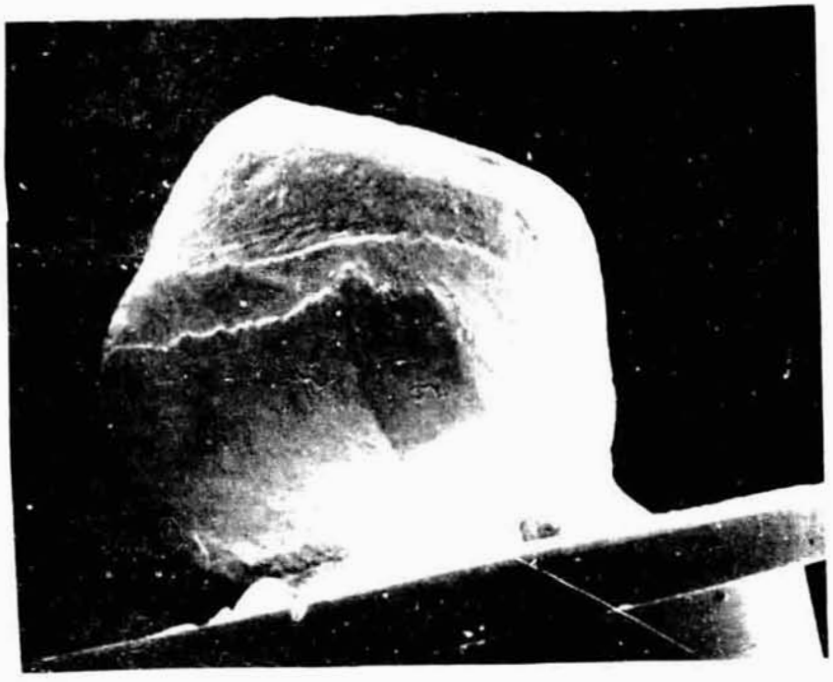

a) Remnant Unmelted Solid/Flat Upper Portion

b) Shallow Cavity on Impact Surface

Fig. 2 Macrophograph of Sample 1-15, Pure Nickel (15×)

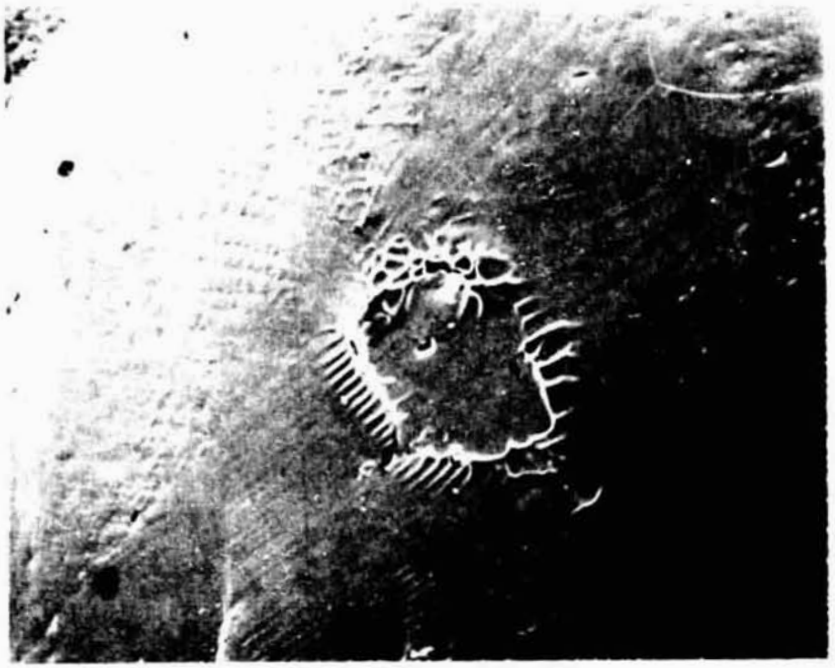

Fig. 3 Shallow Cavity on Surface Following Impact with Chamber Wall While Molten, Sample 1-15, Pure Nickel (150×)

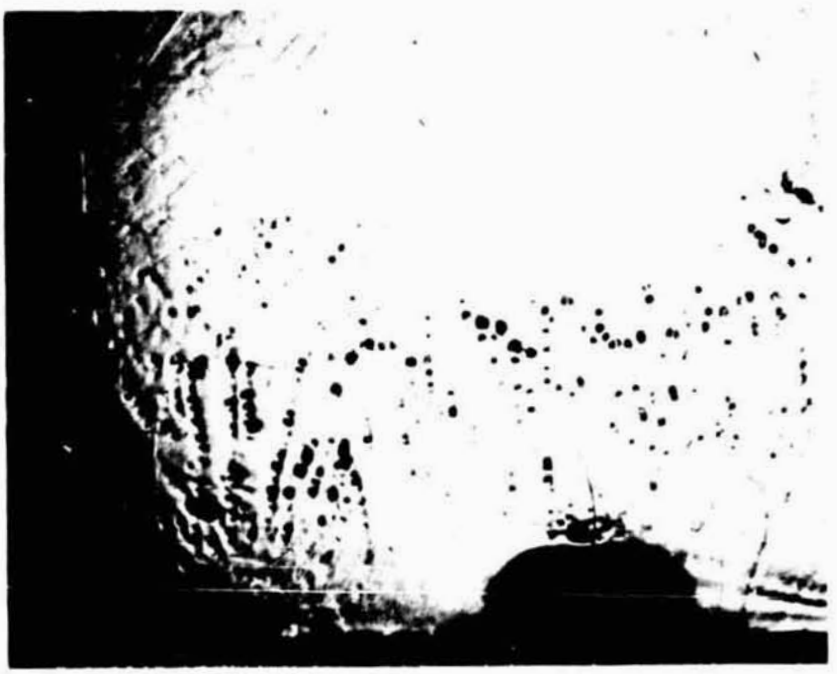

Fig. 4 Microphotograph Showing Cross Section in Vicinity of Impact, Sample 1-15, Pure Nickel (25×)

TABLE 6 ELEMENTAL ANALYSIS OF SURFACES

Sample No.	Region	Nominal Comp (Wt %)	Al	W	Ag	Sn	Ni	Cu	Fe	Cr	Technique
1.2	Avg Side	Pure Ni	6.00	0.05	0.77	0	91.99	0.90	0.17	0	EDAX
	Top	Pure Ni	0.71	0.27	0.31	0	97.41	1.21	0.08	0	EDAX
	Top	Pure Ni	Contamination				100				Microprobe
1.5	Side (Avg)	Ni-12Sn	1.01	0	0.33	5.50	91.72	1.13	0	0	EDAX
	Top	Ni-12Sn	1.04	0.44	0.03	6.74	91.07	0.73	0.12	0	EDAX
	Top (Equiaxed Dendrite)	Ni-12Sn	Contamination			6.06	93.94				Microprobe
	(Dimpled)	Ni-12Sn				7.00					Microprobe
1.7	Side (Avg)	Ni-30Cu	24.59	0	0.26	0.04	62.85	11.67	0.53	0.07	EDAX 0.16
	Top	Ni-30Cu	0.44	0.20	0	0.21	91.92	6.62	0.23	0.38	EDAX 0.07
	Top	Ni-30Cu					90.05	9.05			Microprobe
	Dendrite Arm (Primary)						91.96	8.04			
	(Secondary)						90.36	9.64			
1.13	Side Avg	Ni-1Ag	0.60	0.12	0.06	0.03	97.64	0.83	0.19	0.45	EDAX
1.15	Side (Avg)	Pure Ni	1.97	0	0.62	0.11	96.06	0.76	0.06	0.17	EDAX
	Top	Pure Ni	0.83	0.20	0.59	0.37	96.90	0.66	0	0.45	
2.3	Side (Avg)	Ni-12Sn	21.40	0	19.5	0.88	56.18	1.25	0.44	0.39	EDAX
	Top	Ni-12Sn	2.81	0	1.25	2.09	92.43	1.20	0.21	0	
	Flat Nuclei					6.62	93.38				
	Dendrites (Dimpled)					11.34	88.66				

Figure 4 is a transverse optical micrograph that shows the impact surface, the cellular solidification morphology radiating from this surface, and the incubation distance required for cellular solidification to initiate. At the bottom portion is remnant unmelted solid that has been fully recrystallized by the heating cycle. This region is clearly identified by the large numbers of annealing twins. There appears to have been a small amount of solidification epitaxially from the remnant unmelted solid; however, the primary mode of solidification must be considered cellular, progressing from the impact surface.

Because of the rapid cooling, contamination, and only partial melting, the grain size is appreciably smaller than that of the ground base sample (Table 4). This is not a result of the reduced gravity level of the processing.

Identification of the principal contaminants internally was unsuccessful because most of the contaminant elements seemed to be in solid solution with the Ni. A few isolated particles were located with high silver or aluminum contents. A check of the general contamination level was made by monitoring the Curie point of the sample; it was found that the Curie point was suppressed by some 20°C and this would indicate a contamination level of 1-2 a% total Ag, Al, and Cu. The shape of the Differential Scanning Calorimetry trace was indicative of a low alloy content ferromagnetic material (Ref. 3). Because of rapid cooling, partial melting, level of contamination from the pedestal and from the melting of adjacent samples, it was decided not to pursue the evaluation of this sample further. The physical properties are listed in Table 7 and may be compared with pure Ni data listed in Tables 2 and 4.

TABLE 7 PHYSICAL PROPERTIES

Sample No.	Nominal Comp (Wt %)	Wt (gm)	Specific Wt (gm/cc)	Sphericity (R_{max}/R_{min})	Morphology	Surface Grain Size (mm)	Laue Grain Size (Top) (mm)
1.2	Pure Ni	1.18049	7.21	1.11	Equiaxed	0.09 ± 0.03	~ 0.01
1.5	Ni-12Sn	1.21621	8.87	1.04	Dendritic (2 Dim.)	0.12	> 0.01
					Dendritic (Free)	0.20	
					Dendrite Arm (Primary)	0.012	
					(Secondary)	0.006	
					Interdendritic Void	0.011	
1.7	Ni-30Cu	1.18747	7.64	1.08	Dendritic (2 Dim.)	0.067	~ 0.01
					Dendritic (Free)	0.07 ± 0.05	
1.13	Ni-1Ag	1.16878	6.48	1.44	Equiaxed	0.09 ± 0.03	~ 0.01
					Neck	0.017	
1.15	Pure Ni	1.19475	8.93	1.20	Unmelted Solid	0.031	> 0.01
					Thermal Grooving (Partial Melting)	0.057	
2.3	Ni-12Sn	1.27565	9.25	1.02	Flat Nuclei (Platelets)	0.038	
					Dendrites, 2 Dim.		
					(Dimpled)	0.094	
					(Scalloped)	0.158	
					Dendrites (Free)	0.048	> 0.01

Sample 1-7

Figure 5 is a macrograph of sample 1-7, a Ni-30Cu alloy, that clearly shows the three primary regions of solidification. The lower portion that appears rather smooth, but with some features that appear as vertical lines, is a region of large columnar dendrites that have grown epitaxially from the remnant unmelted solid and heterogeneously from the region of the pedestal. These columnar dendrites progressed rapidly almost halfway into the droplet at which point the ratio of the thermal gradient (G) to growth rate (R) decreased to a critical level and the columnar dendritic growth broke down, resulting in the formation of coarse equiaxed dendrites. The latter dendrites are located in the last regions to solidify and their formation might have been partially associated with convection resulting from solidification shrinkage. These dendrites appear in the mid-region of Fig. 5. The last region to be considered is the uppermost in Fig. 5 and appears as a

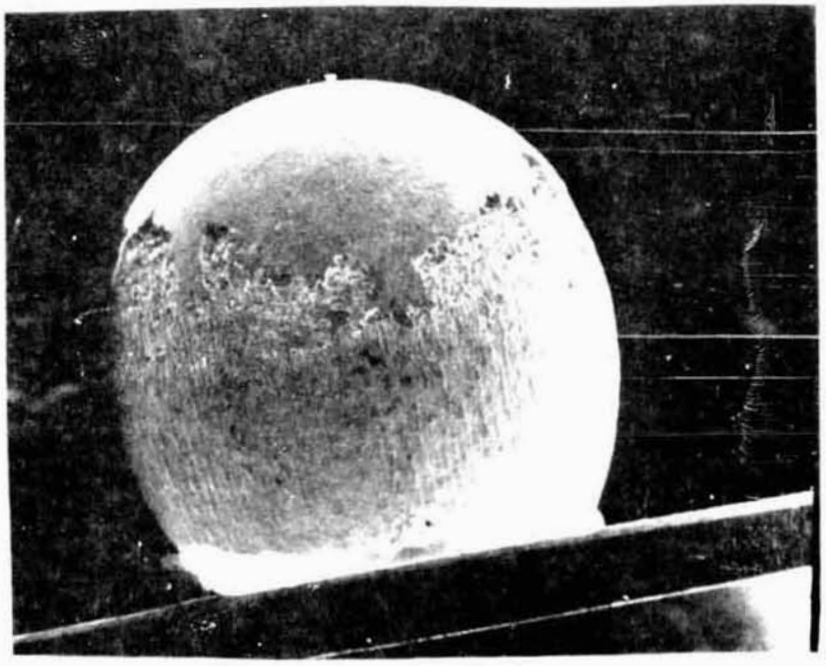

Fig. 5 Macrophotograph of Sample 1-7. Ni-30Cu (15×)

"cap" resting upon the other regions. This cap region is a region of nucleation and growth that occurred on the liquid surface. The nuclei grew both laterally on the liquid surface and radially inward. Because the cap has assumed the macroscopic dimensions of the liquid sphere, its diameter is greater than that of the lower region which is defined by the volume of the solid. This results in a height increment at the interface between the liquid surface nucleated cap and the equiaxed dendrites. This height increment is shown in Fig. 6. In the cap region adjacent to the last region to solidify, there are substantial interdendritic shrinkage cavities and these are shown in Fig. 7. The growth radially inward, of the surface nucleated dendrites, is readily apparent. A transverse section of this region is shown in Fig. 8 and the interdendritic shrinkage cavities are again clearly evident. Figure 9 is an electron microprobe trace that shows the variation of copper content on progressing in a transverse section from the outer "cap" surface radially inward, within a single crystallite. The initially low value of copper may be due to normal evaporative segregation; however, it might also be due to the anticipated "initial transient" on solidification of a crystal of binary material (Ref. 5). If the latter is the case, then the horizontal region would be a region of steady state growth and the first upward swing would be considered the terminal transient. It should be possible to define which of these cases is active and, if the latter, whether the solidification was diffusion or convection limited; but time did not permit such a detailed analysis. It should also be noted that the maximum solute concentration in the first interdendritic region of Fig. 9 is lower than that of the second interdendritic region. This is evidence of the continuing solute enrichment of the liquid as the solidification front advanced.

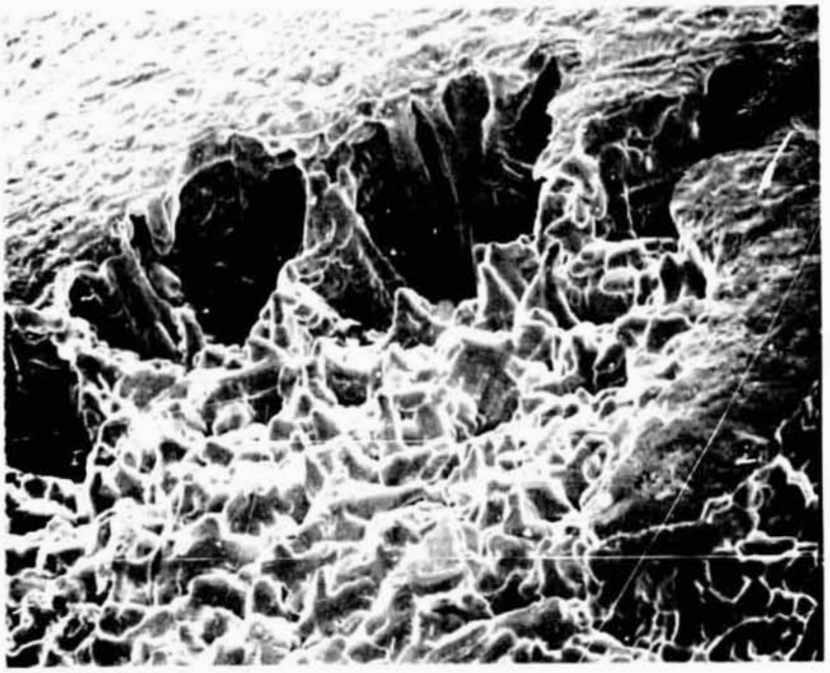

Fig. 6 Region between Cap and Equiaxed Dendrites, Sample 1-7, Ni-30Cu (150×)

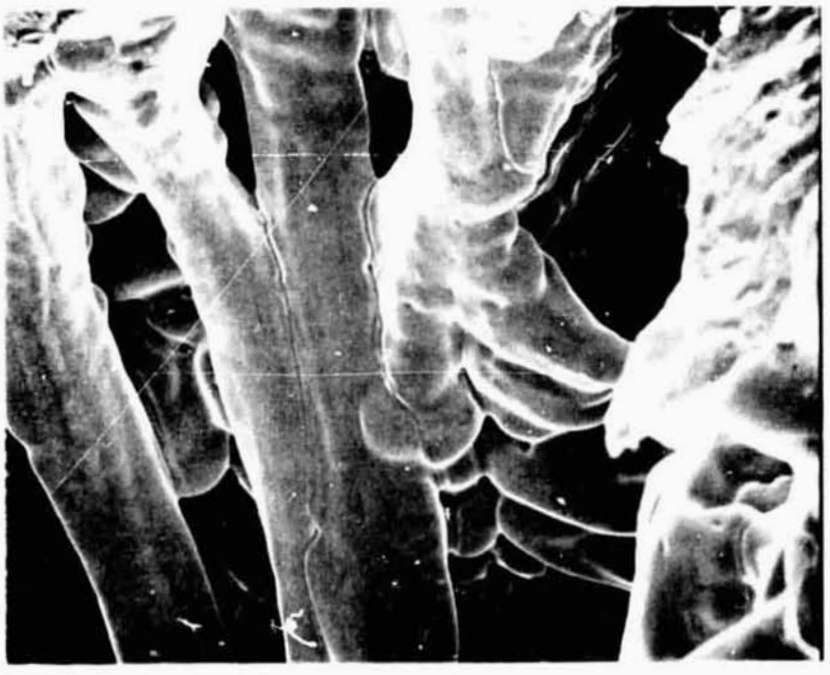

Fig. 7 Interdendritic Shrinkage Cavities, Sample 1-7, Ni-30Cu (375×)

Fig. 8 Microphotograph Showing Transverse Section of Region Shown in Fig. 7, Sample 1-7, Ni-30Cu (100×)

Figure 10 is a microprobe trace of a dendritic array in the region of the equiaxed dendrites. In this region the dendrite solute concentration is not greatly different than the steady state value previously referred to in the cap region. The interdendritic solute content is appreciably higher. This supports the contention that this is close to the last region to solidify, and consideration of the phase diagram (Appendix A) indicates that 40-42 atomic % copper would be the maximum anticipated copper content. The interdendrite arm spacing is substantially greater than in the surface nucleated region.

Figures 11 and 12 are representative of the two surface morphologies found in the cap region. The dendritic morphology of Fig. 12 was predominant and that of Fig. 11 was not documented in the ground base samples. Both of these microstructures were convex

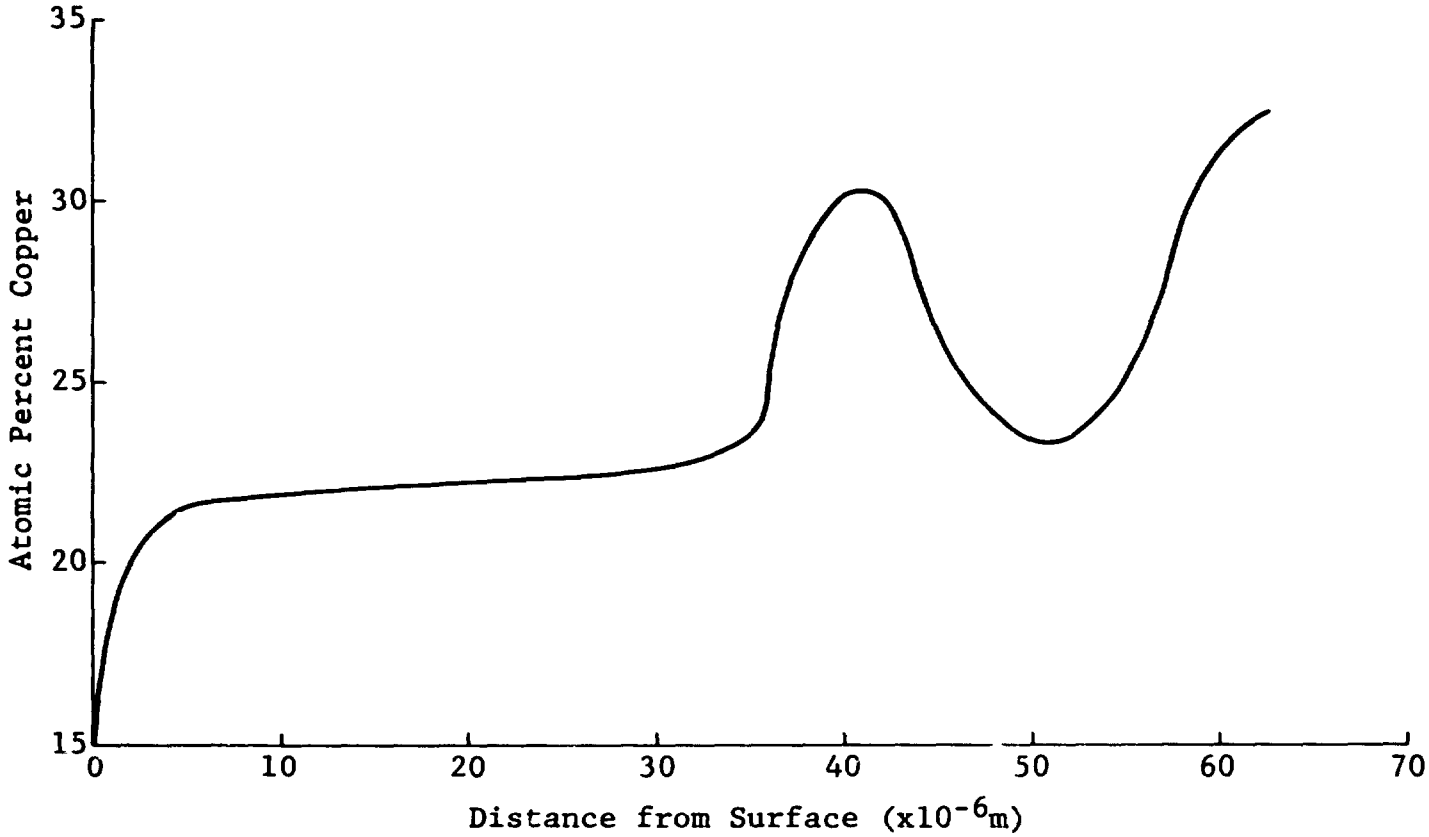

Fig. 9 Variation in Cu Content from Cap Region Inward, Sample 1-7, Ni-30Cu

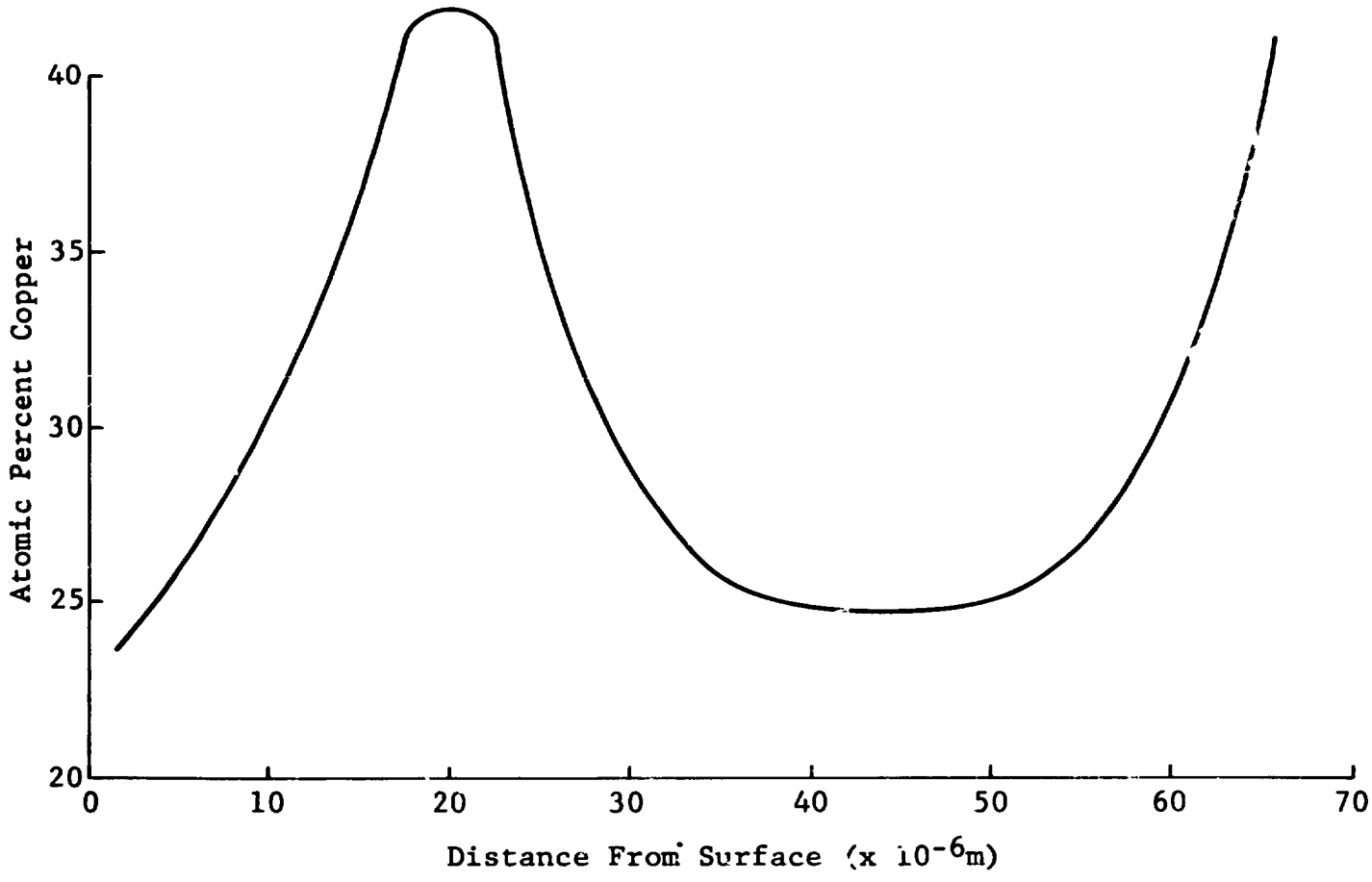

Fig. 10 Variation in Cu Content in the Region of Equiaxed Dendrites, Sample 1-7, Ni-30Cu

Fig. 11 Surface Morphology in Cap Region, Sample 1-7, Ni-30Cu (1500×)

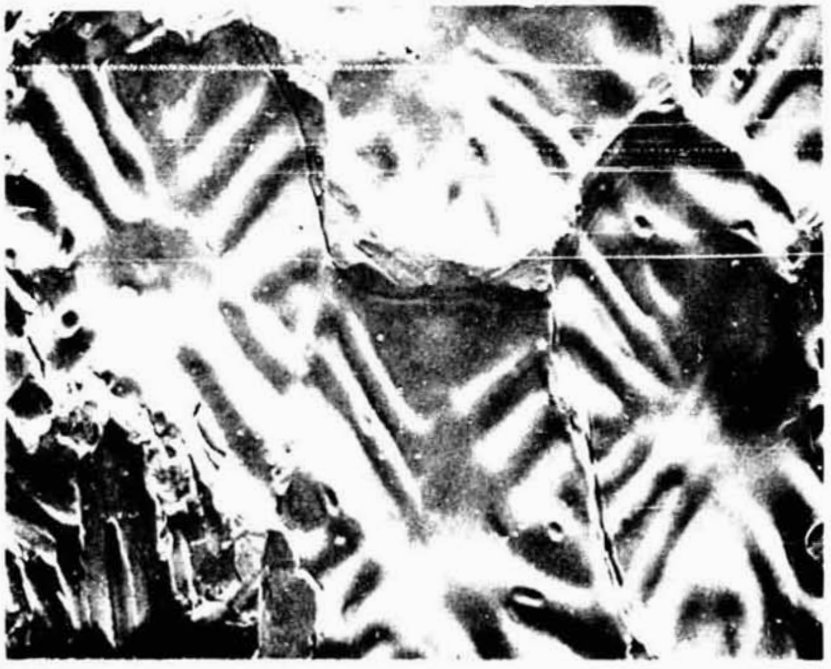

Fig. 12 Dendritic Surface Morphology in Cap Region, Sample 1-7, Ni-30Cu (830×)

inward (concave to the viewer) and this is a result of the requirement that the advancing solidification front must be convex to the liquid. Since the fronts progressed radially inward from this cap region, the grains would appear concave to an external viewer.

Figure 13 is a micrograph of another dendritic grain in the cap region, however, this one is decorated with terraces in some of the last regions to solidify (upper left). This terracing is shown in an enlarged view in Fig. 14. It is not clear at this time if this terracing is due to a last liquid effect, or whether it is due to preferential evaporation of the copper after solidification.

Comparison of the flight sample with the ground base sample indicated that the sphericity was significantly enhanced (1.08 versus 1.29) even though the sample still remained in contact with the Al_2O_3 pedestal and had an appreciable flat at the base. Equiaxed dendrite grain size measurements were comparable, and the grain size measured at the surface, in the cap region, was also comparable (0.07 mm versus 0.010 mm) when the sampling errors and statistics are considered. Microstructurally, one difference that did seem beyond the errors in sampling was the size of the columnar grains found in both the ground base and flight samples. In the case of the ground base samples these were typically 0.8 x 0.2 mm whereas in the flight sample they were 4.0 x 1.4 mm. This is not thought to be due to the weightless environment, but rather to the higher degree of total melting that the flight sample experienced, thus reducing the number of available heterogeneous nuclei present as remnant unmelted solid or within the pores of the pedestal surface. The interior lattice parameter was 3.5500Å for the flight sample and 3.5544Å for the ground base sample. This might indicate a slight reduction in the total copper content due to the longer heating time and preferential evaporation of the copper species; however, it was not an appreciable difference.

Fig. 13 Dendritic Grain in Cap Region, Showing Terraces, Sample 1-7, Ni-30Cu (750x)

Fig. 14 Terraces in Cap Region, Sample 1-7, Ni-30Cu (3750x)

Curie point measurements indicated that because of the continuous variation of copper content, the only point measurable with a high degree of certainty was the Curie point associated with the minimum copper content. This was found to be 247°C, which is comparable to an alloy with approximately 10 percent copper. This must be associated with the cap region where the bulk analysis indicated 9.05 percent copper, with variations from 7.82 to 11.53 percent.

We may thus conclude that the physical and microstructural aspects of this sample were analogous to those previously measured for the ground base sample. Any differences noted were more readily attributed to differing thermal conditions during melting and solidification than to the reduced gravity environment.

Not directly related to the alloy in question, but consistent with the previous sample, was a substantial level of surface contamination of aluminum, from the pedestal. This level of contamination did not seem consistent with that measured for the ground base sample (see Table 6). This, too, may have been associated with the higher temperature of the Skylab processing, but should be noted, nevertheless.

Samples 1-5 and 2-3

Samples 1-5 and 2-3 were nominally Ni-12 wt% Sn and both showed extremely high degrees of sphericity (1.04 and 1.015, respectively). These values are to be compared with values of 1.29 and 1.50 for the ground base samples. Sample 1-5 is shown macroscopically in Fig. 15 and has a small flat at the base where it had remained in contact with the Al_2O_3 pedestal. This small flat resulted in the sphericity value being as high as 1.04. It would otherwise have been better.

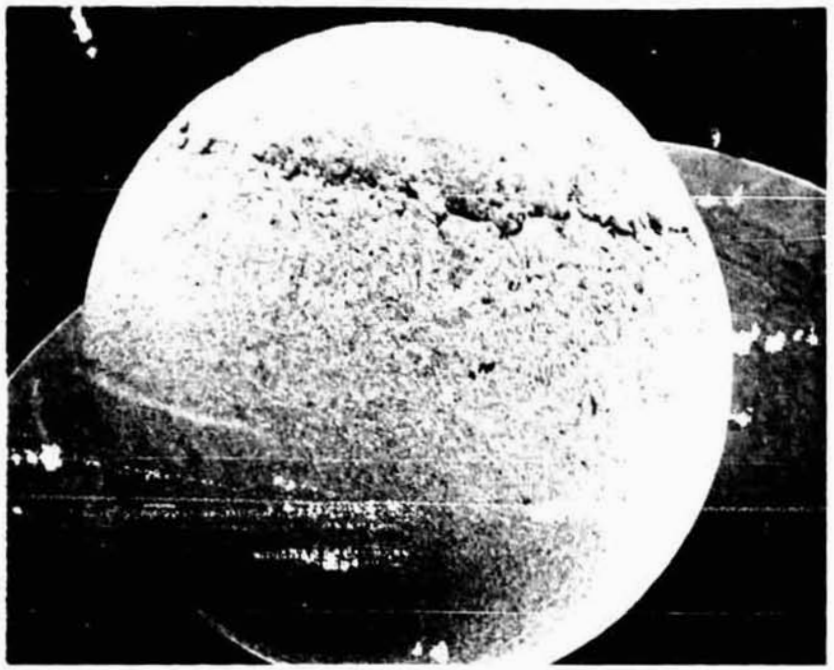

Fig. 15 Macrophotograph of Sample 1-5, Ni-12Sn (15x)

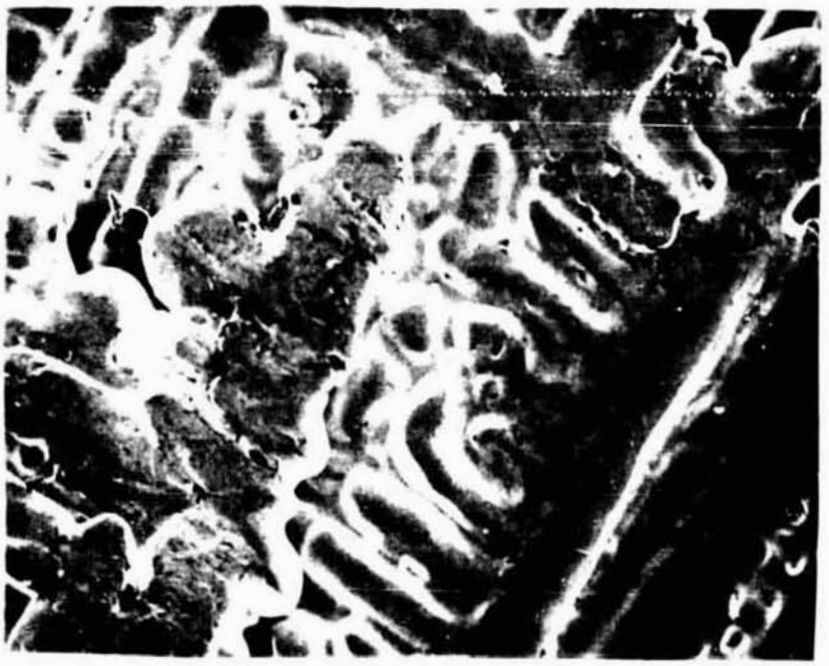

Fig. 16 Columnar Dendrites, Sample 1-5, Ni-12Sn (1000x)

The solidification of this sample is analogous to the previous sample (1-7) in that there are three principal regions of solidification. The lower region was characterized by large columnar dendrites radiating from the remnant unmelted solid, and from the pedestal region, and these changed to epitaxial dendrites as the value of G/R decreased, as previously noted. These columnar dendrites are shown in Fig. 16. The columnar dendrites were superseded by equiaxed dendrites in the mid-range of Fig. 15 and the solidification of the uppermost portion of Fig. 15 is characteristic of surface nucleated solidification. The height increment at the interface between the surface nucleated and equiaxed dendrites is not as apparent in this material, and may indicate a substantially reduced volume difference between the liquid and the tin expanded nickel lattice. This region is shown in Figs. 17 and 18. Figure 17 shows equiaxed free dendrites that have been exposed, in this last region to solidify, by interdendritic solidification shrinkage, and Fig. 18 shows the surface nucleated dendrites that are prominent because of the same shrinkage cavities.

Figure 19 is a macrophotograph of sample 2-3. The high degree of sphericity is readily apparent and it should also be noted that there is no clearly defined surface nucleated/equiaxed dendrite interface. This is because this sample was retained on a fine "sting" that acted only as a point source of heterogeneous nucleation, rather than the previously documented extensive regions of heterogeneous nucleation that resulted in extensive regions of epitaxial columnar dendrites in the other samples. The cap region of surface nucleation has extended over the majority of the sample surface.

Figure 20 is a micrograph representative of the surface of sample 2-3. The region shows two distinctly different morphologies. Toward the lower left portion is a series of flat grains, somewhat

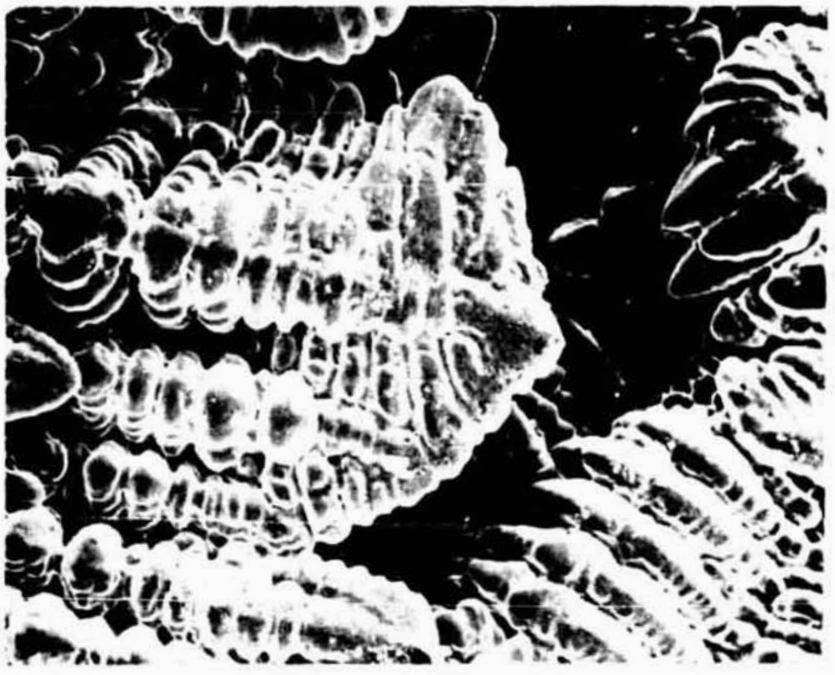

Fig. 17 Equiaxed Free Dendrites in the Last Region to Solidify, Sample 1-5, Ni-12Sn (375×)

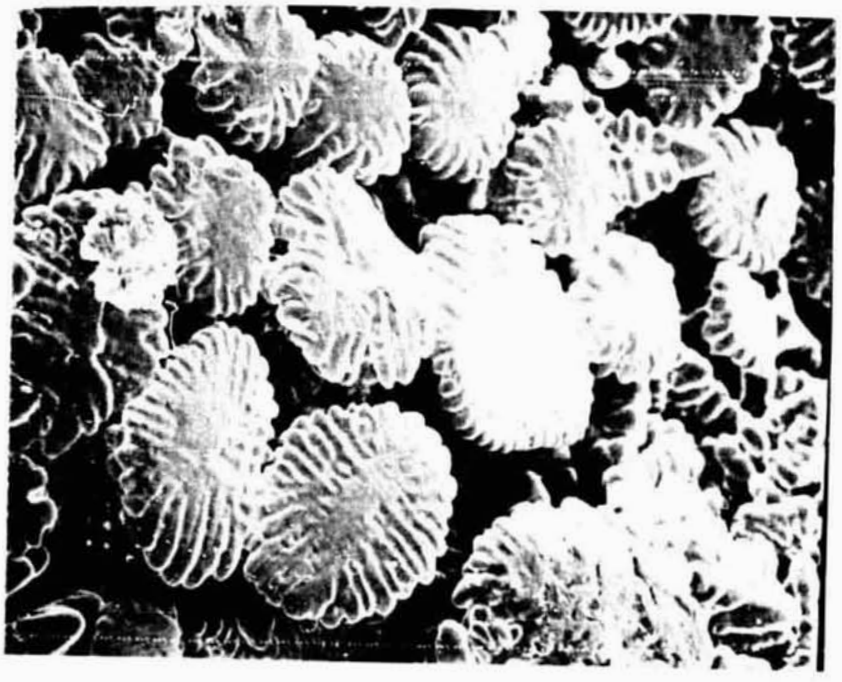

Fig. 18 Surface Nucleated Dendrites, Sample 1-5, Ni-12Sn (200×)

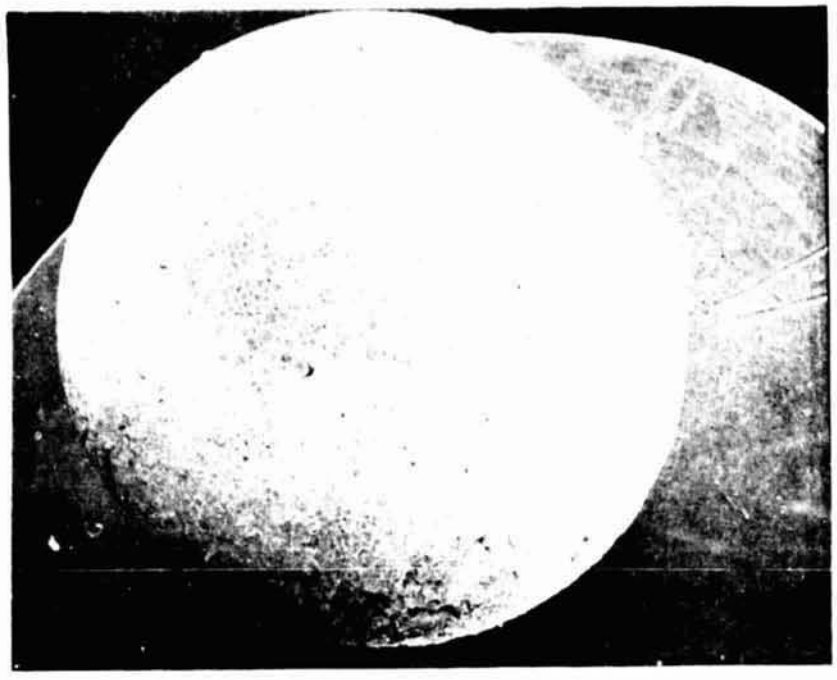

Fig. 19 Macrophotograph of Sample 2-3, Ni-12Sn (15×)

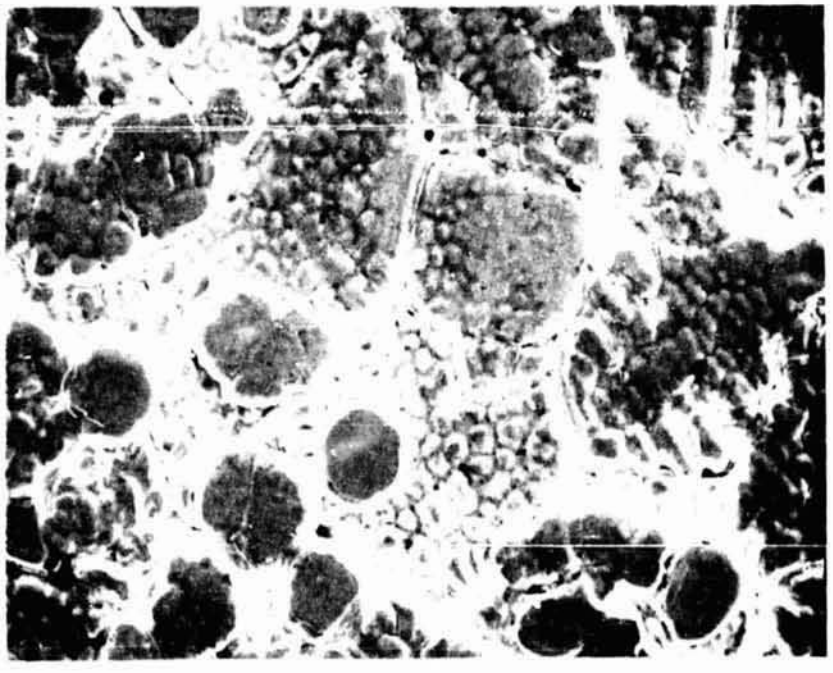

Fig. 20 Surface Morphology Showing Platelet and Cellular Microstructures, Sample 2-3, Ni-12Sn (375×)

hexagonal in shape, representative of platelet solidification. These were raised above the more extensive cellular microstructure and were formed first. Figure 21 is an enlargement of the platelet structure, the elevation is apparent, and varying degrees of terracing toward the outer edges is evident. These platelets were formed while the G/R ratio was very high.

Fig. 21 Platelet Surface Morphology, Sample 2-3, Ni-12Sn (3375×)

Figure 22 is an enlargement of the cellular microstructure that formed as the G/R ratio decreased; each of these cells is also clearly terraced. The origin of this terracing is uncertain at this point. Figure 23 is representative of some regions of the surface of sample 2-3. This seems to be somewhat of a degenerate microstructure in that some of its aspects appear cellular whereas others appear dendritic and it is included here for purposes of documentation. Equiaxed dendritic arrays were found in some of the last regions to solidify, but these were similar to Fig. 17

Fig. 22 Cellular Surface Morpholcgy, Sample 2-3, Ni-12Sn (3375×)

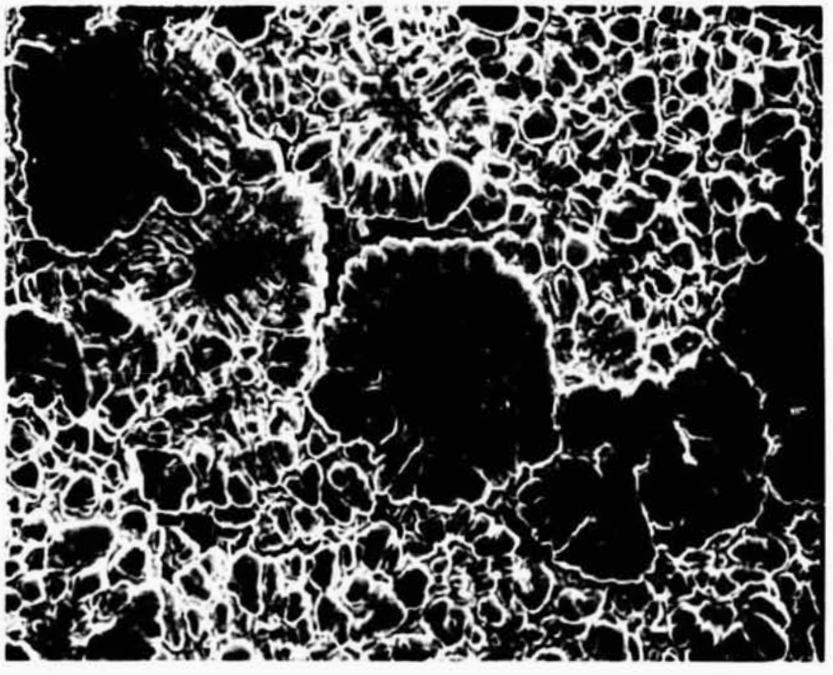

Fig. 23 Degenerate Surface Morphology, Sample 2-3, Ni-12Sn (200×)

and are not reproduced here. Some of the last regions to solidify in this sample also showed appreciable decoration by the second phase Ni_3Sn particles. This is shown in Fig. 24. It should be noted that the precipitate particles are not randomly situated in interdendritic interstices, as might have been anticipated, but are arrayed on the dendrite arms in highly localized patterns that in some cases were {100} ⟨110⟩ crystallographic systems.

An additional feature of the dendrites that could only be resolved at high magnifications was terracing on the tips of primary and secondary dendrite arms. These terraces were on the {111} faces, the leading faces, of the dendrite tip. Figure 25 is an example of a primary dendrite tip with a primary spiral that appears to be interacting with two secondary dendrite spirals. This is shown in an enlarged view in Fig. 26.

Both the localized solute redistribution and the growth terraces are outstanding records of their type and were not documented for the ground base samples. Further, the platelet and cellular surface morphologies shown in Fig. 20 are not typical of the ground base samples. The latter condition is probably due to a variation in the thermal conditions (G and R) for sample 2-3, rather than a fundamental difference due to the reduced gravity environment.

A comparison of the metallurgical features of the flight samples with the ground base samples (Table 4) indicates that the surface nucleated dendrites of the flight samples (Table 7) varied from 0.09 mm to 0.16 mm whereas the ground base regions were typically 0.14 mm to 0.15 mm; essentially identical. Equiaxed dendrites within the samples were typically 0.20 mm in flight sample 2-3 and 0.15 mm for the ground base samples. This, too, is essentially the same when the high heat input to sample 2-3 is considered.

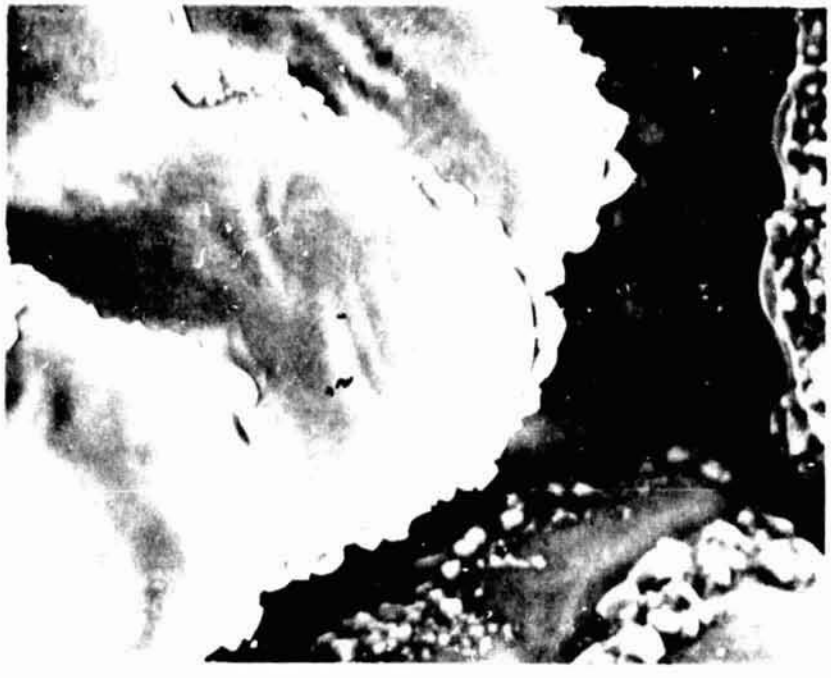

Fig. 24 Decoration of Dendrite Arms in Last Regions to Solidify by Ni_3Sn Particles, Sample 2-3, Ni-12Sn (1500×)

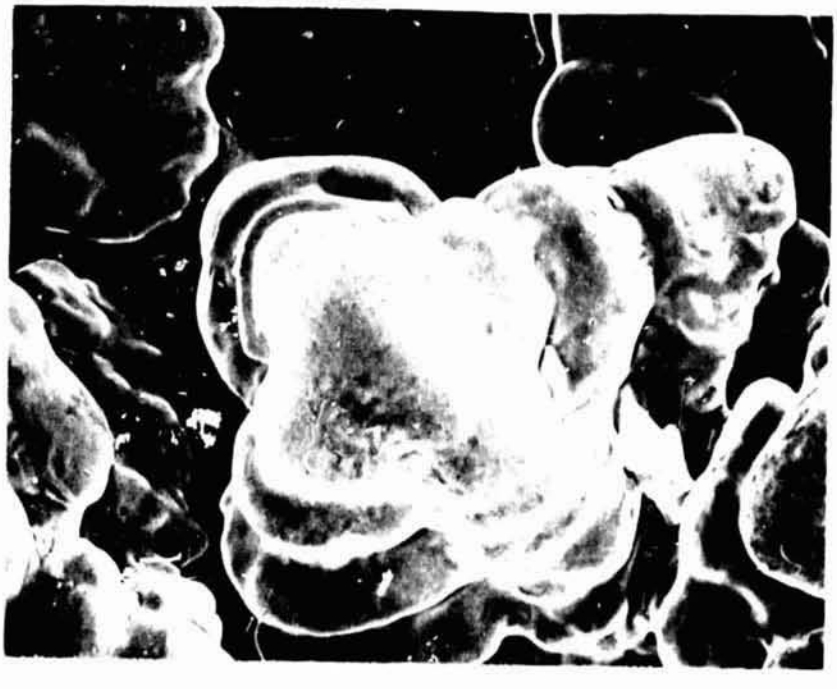

Fig. 25 Terraces on Dendrite Arm Tips, Sample 2-3, Ni-12Sn (3750×)

Fig. 26 Figure 25 at High Magnification, Sample 2-3, Ni-12Sn (7500×)

Since the alloy in question is a hypoeutectic alloy (see Appendix A), the anticipated solidification sequence is such that as freezing begins the first crystals to form are appreciably solute (tin) depleted. As solidification proceeds, the composition of the liquid follows the liquidus and the composition of the solid follows the solidus, as in the freezing of an isomorphous alloy. This process is interrupted, however, and the remaining liquid of eutectic composition freezes isothermally to a eutectic mixture. Thus, the solidification sequence is such that the liquid undergoes a univariant transformation as well as bivariant transformation.

Samples of the tin concentration in the first regions to solidify indicated a minimum tin concentration of 4.25 wt% in the

platelet, columnar dendrite, and equiaxed dendrite regions. The maximum value was 15.56 wt%. Interdendritic compositions varied from a low of 22.86 wt% to a high of 32.42% (the eutectic composition). The highest segregation ratios monitored were 9.91 on sample 2-3 and the lowest was 2.69 on sample 1-5.

Solidification was principally dendritic internally and this is shown in Fig. 27, for sample 2-3. Remnant unmelted solid, from the sting, is shown at the bottom and columnar dendrites are shown radiating from this region. The columnar dendrites then decay to equiaxed dendrites as the G/R ratio decreases. This regular dendritic array was noted throughout specimen 2-3 and in parts of specimen 1-5. Specimen 1-5 was predominantly an irregular array of what may be termed primary dendrites, as shown in Fig. 28. The eutectic mixture is in the interdendritic regions in both cases, however, it is almost a divorced eutectic and this is shown in Fig 29.

Although platelet, cellular, and dendritic solidification has been detailed on the surfaces, and the interiors have been noted to be almost exclusively dendritic, the importance of G and R in selecting the solidification mode cannot be overemphasized. Figure 30 is a plot of the variation of microchemistry of primary crystals with distance and Table 8 tabulates the data for the various modes of solidification on the surfaces and within both samples. The microchemical variation is essentially the same, within each of these primary crystallization regions. This emphasizes that the thermal parameters are dominant and the compositional variation is a dependent variable. The thermal parameters determine the mode of solidification and if the sampling is conducted in equivalent $\langle 100 \rangle$ directions, the compositional variation will be equivalent.

Fig. 27 Region Where Solidification Started, Sample 2-3, Ni-12Sn (100×)

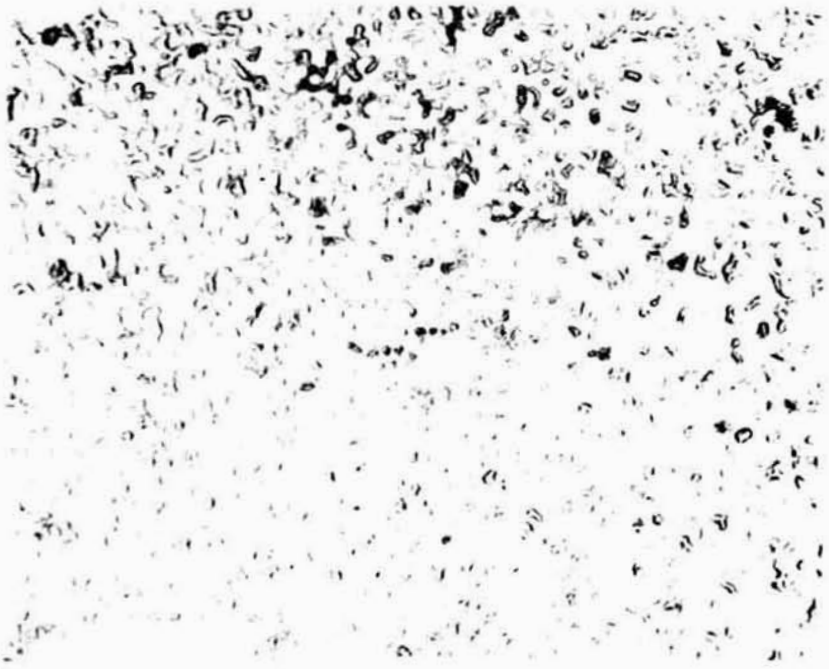

Fig. 28 Primary Dendrites, Sample 1-5, Ni-12Sn (100×)

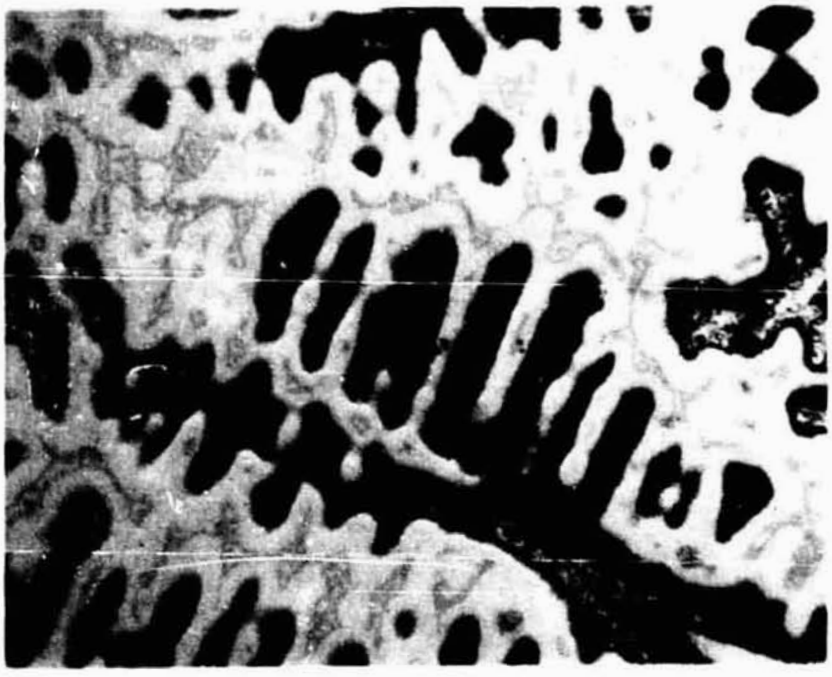

Fig. 29 Eutectic in Interdendritic Region, Sample 1-5, Ni-12Sn (500×)

The dendritic solidification results in tin-rich and depleted regions of the samples, as previously explained. This was reflected in the lattice parameters. Samples 2-3 and 1-5 had solute-rich parameters of 3.6000Å and 3.5993Å, respectively, whereas the solute-depleted parameters were 3.5783 and 3.5779.

The ground base results gave lattice parameters of 3.608 and 3.611 and solute-depleted values of 3.548 and 3.552. The mean bulk parameters for all of the samples were 3.5783 (sample 2-3), 3.5779 (sample 1-5), and 3.578 and 3.582 for the ground base samples. This would seem to indicate that the microstructure typical of sample 1-5 (Fig. 28) exhibits reduced lattice parameter spread, resulting from a reduced segregation ratio.

Lastly, the Curie points were monitored for samples 1-5 and 2-3 and were found to be 189 and 175°C, respectively. This is

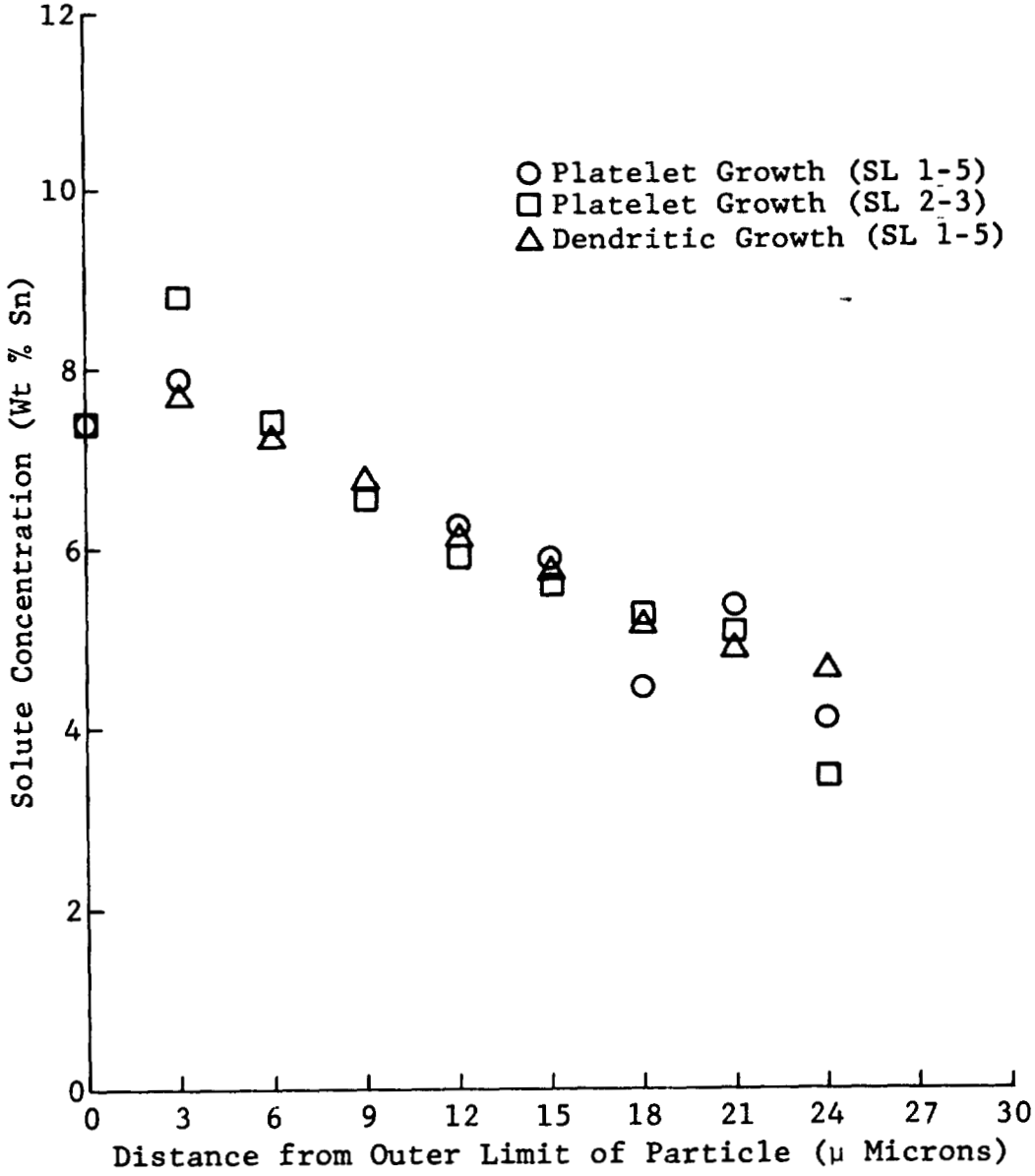

Fig. 30 Variation of Sn Content with Growth Morphology, Samples 1-5 and 2-3, Ni-12Sn

TABLE 8 VARIATION OF SOLUTE CONCENTRATION WITH DISTANCE FOR SAMPLES 1-5 AND 2-3 VARYING MODES OF SOLIDIFICATION

	Solute Concentration (Wt% Sn), ⟨100⟩ Direction		
Distance (μ)	Platelet (S.L. 1-5)	Platelet (S.L. 2-3)	Dendritic (S.L. 1-5)
0	7.40	7.39	5.97
3	7.87	8.82	7.69
6	7.20	7.38	7.21
9	6.77	6.49	6.77
12	6.24	5.89	6.12
15	5.87	5.57	5.70
18	4.43	5.23	5.14
21	5.35	5.06	4.83
24	4.11	3.45	4.60
27			
30			
	Surface	Interior	Interior

substantially higher than the 108°C Curie point measured for the as-received material. This is probably an indication that there has been appreciable tin loss during processing. Since tin has a higher vapor pressure than nickel at these temperatures, this is to be expected, due to normal evaporative segregation.

In summary, then, we have demonstrated the importance of careful control of the thermal parameters in determining the resultant sample morphologies. Apart from thermal considerations, however, there is an outstanding record of solidification and some surprising results with respect to crystallographic localization of the rejected solute. These aspects are not clearly identified with

the weightless processing, however, the reduced gravity environment might be playing an indirect role here, perhaps in limiting convective mixing and thereby magnifying effects that would be tied to a diffusional solution to the solidification equations. This should be pursued in subsequent investigations.

Samples 1-2 and 1-13

These samples were nominally Ni-1 wt% Ag which is a hypomonotectic composition (see Ni-Ag, Appendix A), according to the accepted phase diagram. A hypomonotectic alloy, on freezing, passes through a state of bivariant equilibrium before the univariant monotectic reaction occurs. Freezing begins with the promonotectic nucleation of the terminal nickel solid solution until the monotectic temperature is reached, at which point the monotectic reaction occurs, yielding the secondary monotectic constituent. On further cooling the secondary monotectic constituent, in this case a silver-enriched liquid, undergoes further bivariant reaction and then goes through another univariant solidification reaction that is, in this case, a eutectic reaction. This completes the solidification process.

This solidification sequence was the anticipated one, however, the samples behaved somewhat differently than expected. Figures 31a and 31b show macroscopic views of sample 1-2 and Figs. 32a and 32b are macroscopic views of sample 1-13. Clearly, both samples are highly distorted from the anticipated spherical symmetry.

The outer surface morphologies of these samples were not the clearly cellular solidification patterns documented on the ground base samples. No real evidence for lateral cell formation at the surface was noted, nor was there any evidence of the "pox" noted on the ground base samples (Ref. 4). The surface was significantly

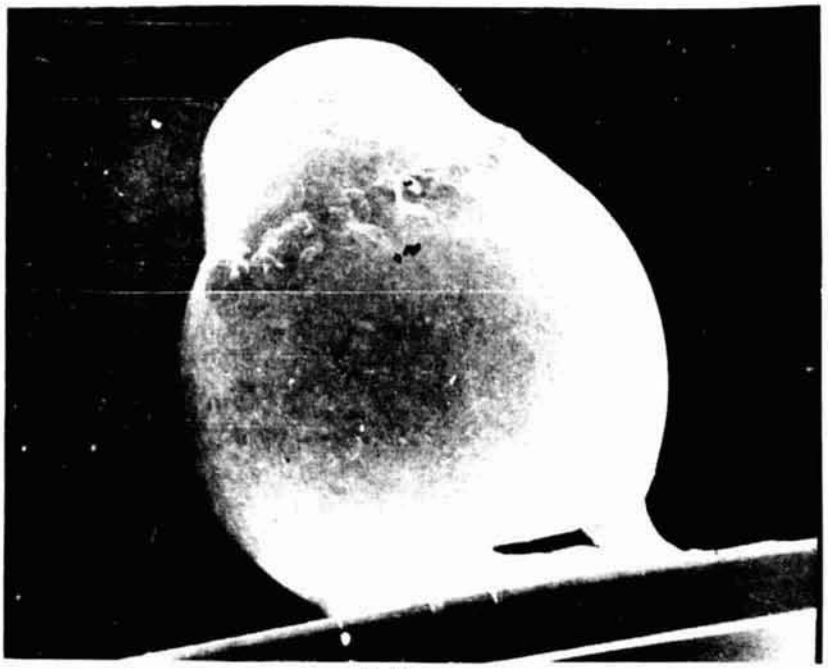

(a)

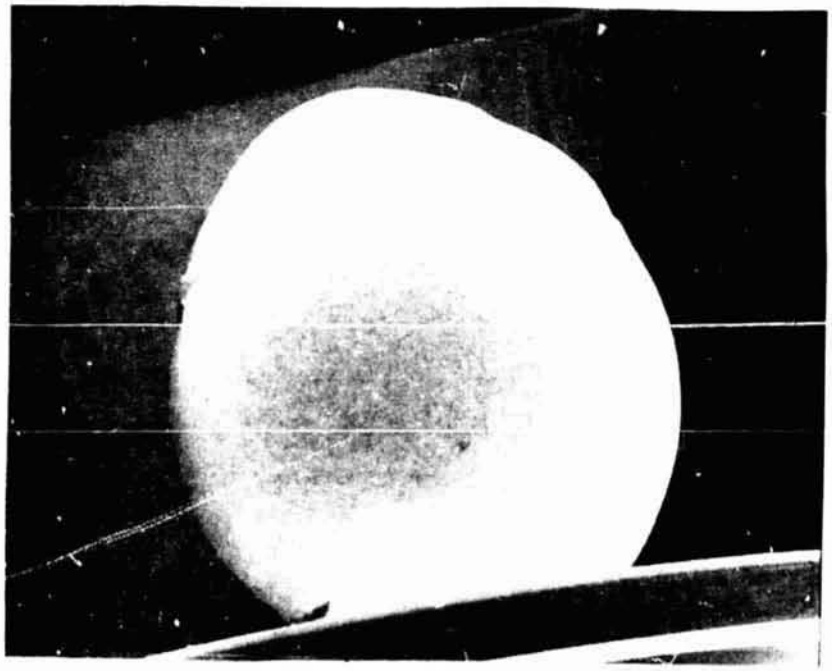

(b)

Fig. 31 Macrophotographs of Sample 1-2, Ni-1Ag (15×)

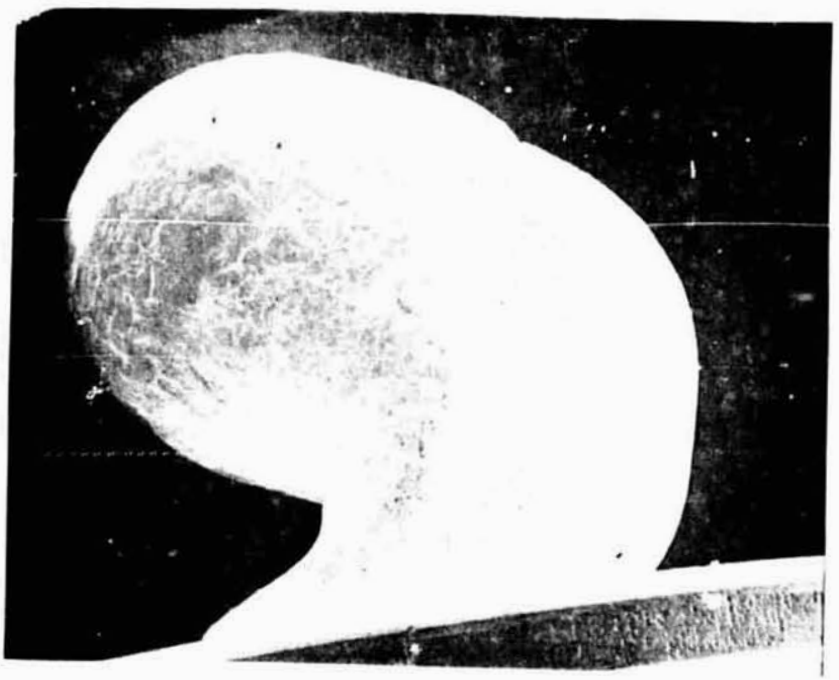

(a)

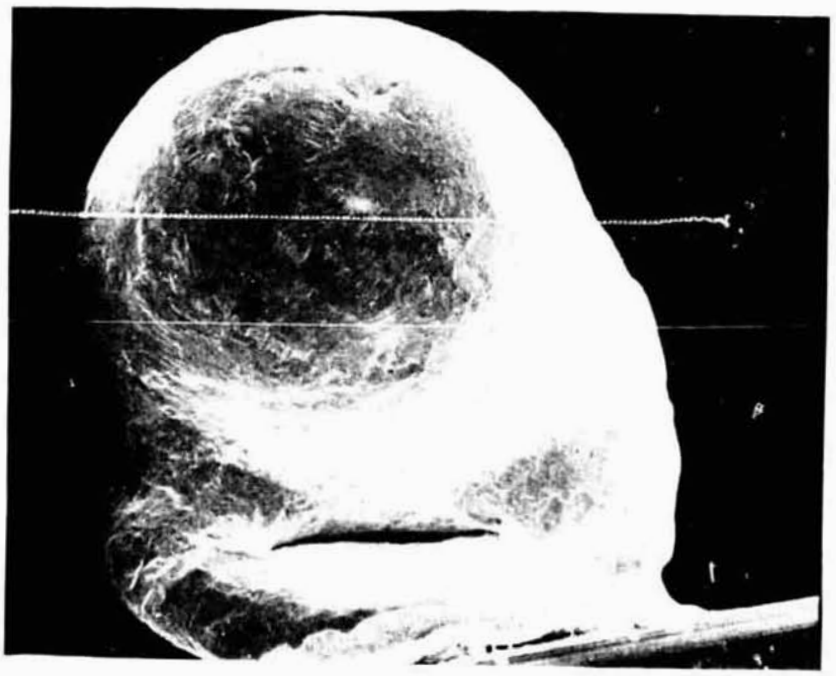

(b)

Fig. 32 Macrophotographs of Sample 1-31, Ni-1Ag (15×)

more faceted than might have been anticipated and a representative area of the surface of sample 1-13 is shown in Fig. 33.

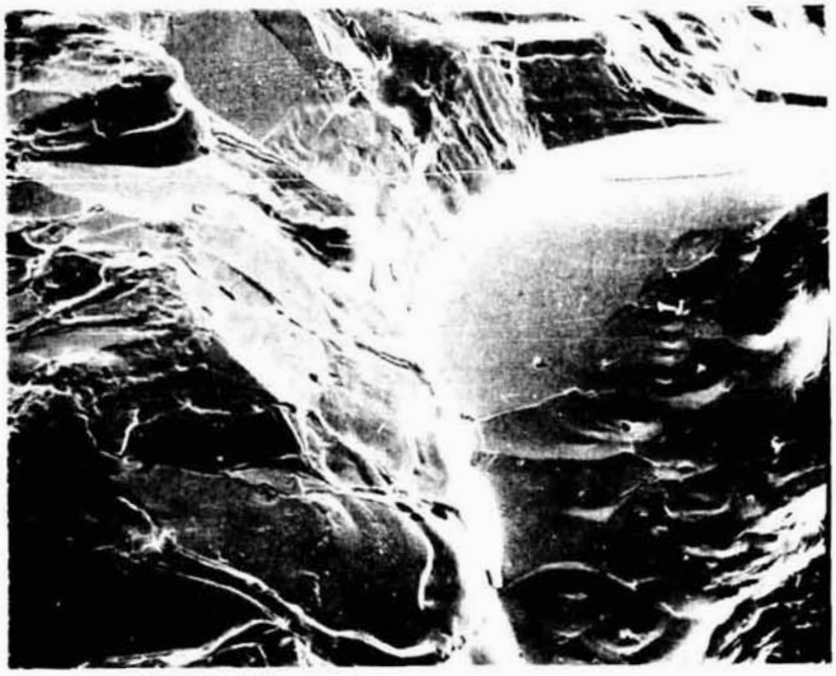

Fig. 33 Faceted Surface, Sample 1-13, Ni-1Ag (150×)

If Fig. 32a is considered in some detail, note that there is a large area of remnant unmelted solid to the right and a large dome that projects to the upper left. This sample had been only partially melted on its first exposure to the electron beam and astronaut Pete Conrad decided to remelt the specimen with another exposure to the beam. On impingement of the beam for the second time, the previously partially melted solid did not melt and spheroidize as anticipated, but rather the molten portion lifted from the cooler base, leaving a viscous separation pattern on the plateau region under the dome. This viscous flow is shown in Fig. 34. Presumably, the mating viscous flow pattern on the lower side of the dome was absorbed into the fully molten dome region.

The asymmetric regions of these samples were found to be hollow both by radiographic techniques and on subsequent sectioning

Fig. 34 Viscous Flow Region, Sample 1-13, Ni-1Ag (750x)

Fig. 35 Cavities within Sample 1-2, Ni-1Ag (36x)

of the samples. The dome region of Fig. 32a was found to be totally hollow, with a shell of solidified liquid metal encompassing a cavity that extended all the way back to the remnant unmelted solid. There are two cavities within sample 1-2 and these are shown in Fig. 35. The morphology of the inner surfaces of the cavities is varied and both platelet and dendritic arrays could be seen throughout the lower cavity, whereas the upper surface of the web region is of a classically cellular morphology (shown enlarged in Fig. 36).

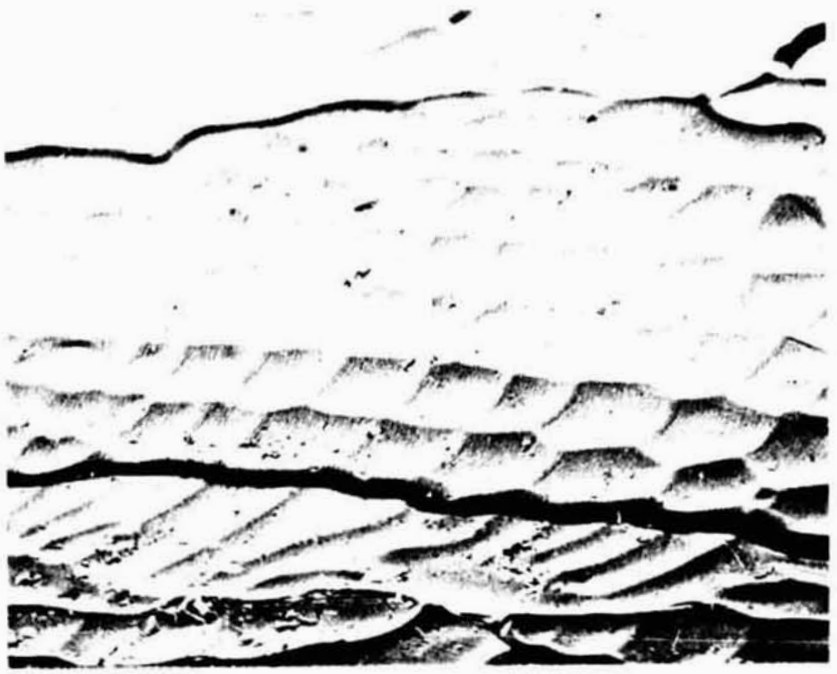

Fig. 36 Cellular Morphology within Cavity, Sample 1-2, Ni-1Ag (1500×)

Also of interest within the upper cavity is evidence that the cavity was formed after the outer shell was in a solid condition. Evidence of this was in the form of slip lines that appeared throughout the grains of the web and the upper shell. These slip lines are shown in Fig. 37 and should not be mistaken for {111} terracing, even though the slip lines were confirmed to be {111} planes by

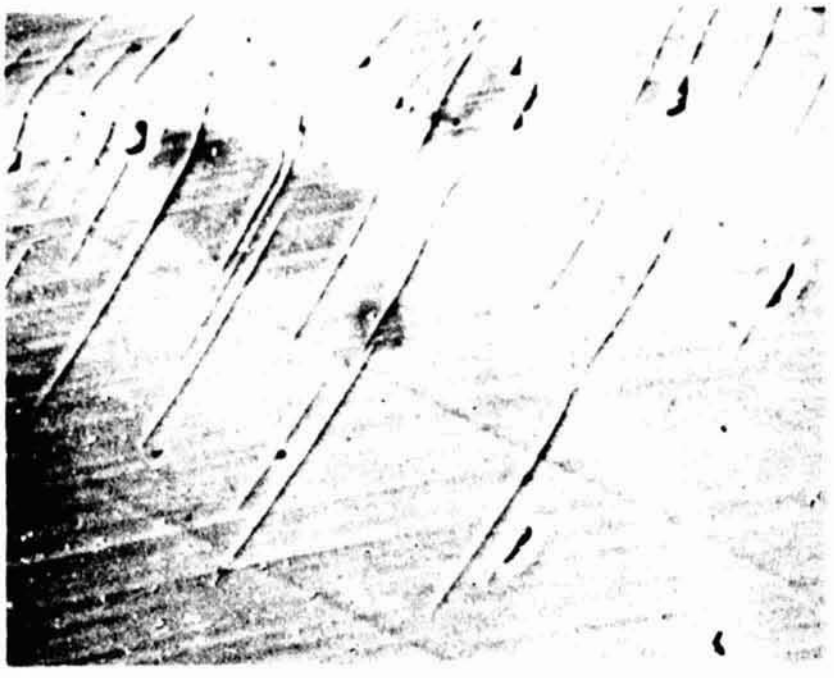

Fig. 37 Slip Lines in the Cavity of Sample 1-2, Ni-1Ag (3750×)

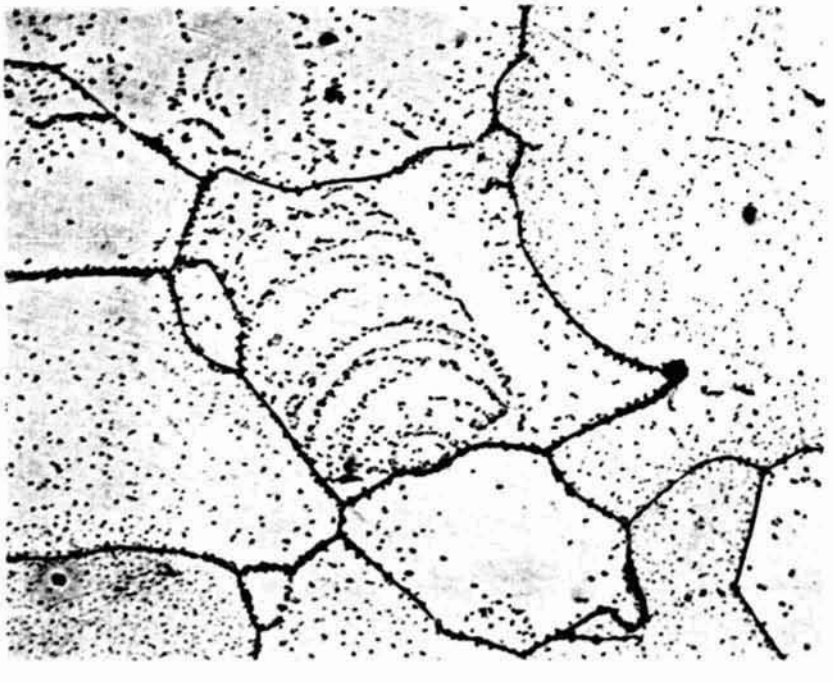

Fig. 38 Internal Microstructure Showing Features Decorated by Ag Precipitates, Sample 1-2, Ni-1Ag (200×)

the single surface analysis technique of Ref. 6. This can be definitively confirmed if all four {111} variants can be detected in the same planar grain, as opposed to the maximum of three variants possible for a planar solidification artifact.

Solidification in these samples was not strictly of the cellular type found in the ground base samples. Silver particles were uniformly distributed throughout polygonal grains and were not confined to a restrictive cellular pattern. Figure 38 shows a representative internal grain microstructure; however, the origin of the decorated spiral source-like array is unknown at this time.

Consideration of why the cavities formed in the Ni-1Ag alloys as well as in some of the Ni-12Sn flight samples has led to careful consideration of the parameters involved in the processing. This, in turn has led us to consider Pressure (P), Temperature (T), and Composition (X) diagrams and Pressure (P) Temperature (T) projections for the Ni-Sn and Ni-Ag systems. The P-T projection for Ni-Ag is presented in Fig. 39. The phase diagram presented in Appendix A and utilized in planning the experimentation is representative of an isobaric section taken at approximately P_1 on Fig. 39. This corresponds to 1 atmosphere of pressure at 1-g. The flight experiment, however, was conducted at a reduced pressure of 10^{-5} mm Hg and a reduced gravity level. This has resulted, on detailed consideration, in two demonstrable effects due to the reduced gravity environment. First, the reduced gravity level greatly reduced the hydrostatic pressure head within the liquid droplet and has resulted in transposing the reduced pressure isobaric sections from the realm of academic exercise to a matter of practical consideration of gas/liquid/solid reaction rather than the terrestrially anticipated liquid/solid reactions. Second, the metallic gases formed in these reactions

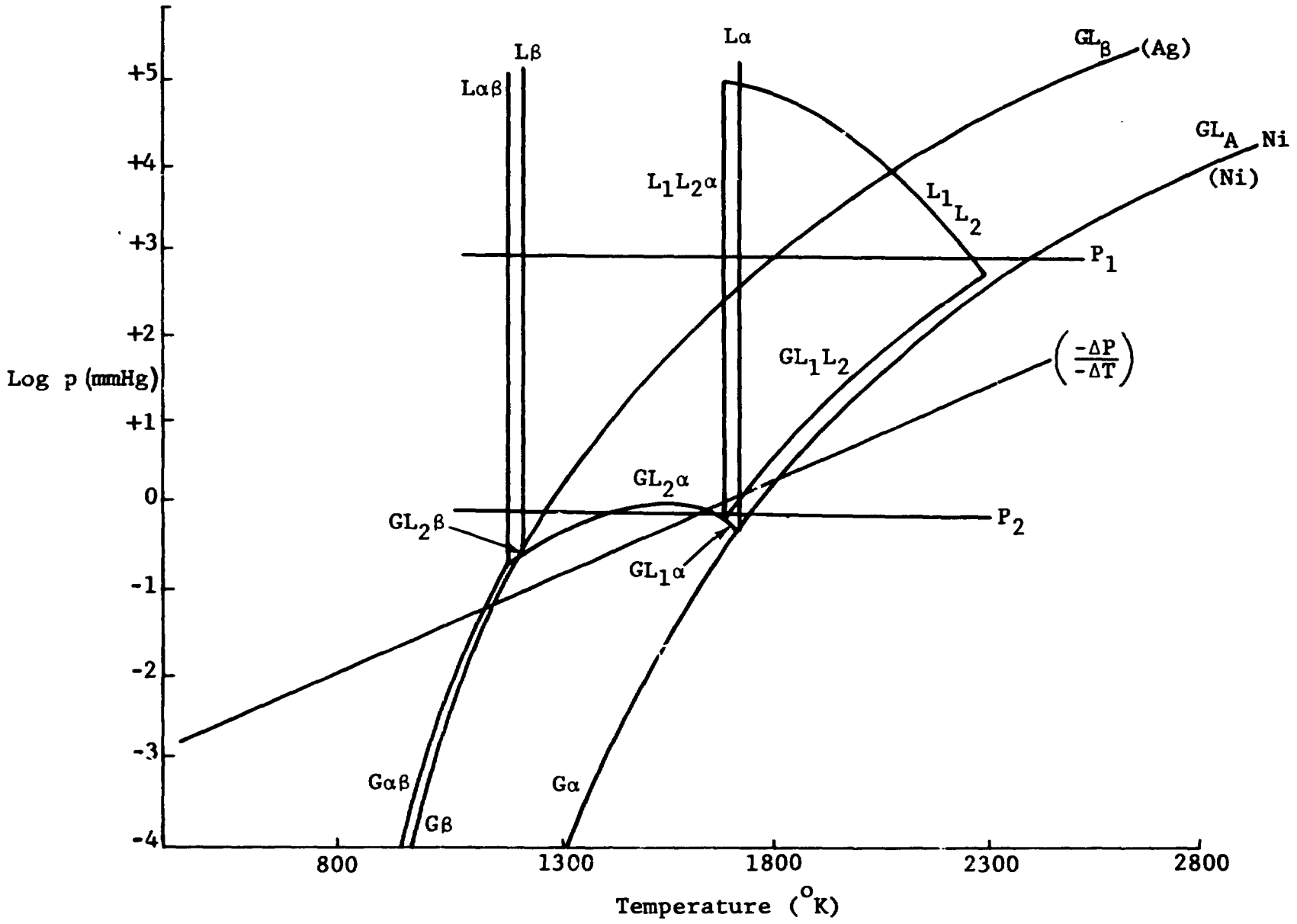

Fig. 39 Pressure-Temperature Diagram for Ni-Ag

are geometrically stable because there is substantially no difference in specific weight between the gaseous and liquid or solid components. This gives the gas no buoyancy force with which to geometrically evolve from the droplet once it has formed. Further, the droplet configuration is such that solidification occurs from the outside and progresses inward and in this fashion the gases evolved are entrapped by yet another process.

Specific consideration of reduced pressure isobaric sections of the P-T projection shown in Fig. 39 or in a section derived from a continuously decreasing pressure (- ΔP) with decreasing temperature (- ΔT), both result in a T-X phase relationship that is shown, purely qualitatively, in Fig. 40. Consideration of the solidification sequence for this type of phase diagram and a hypomonotectic composition shows that the secondary monotectic constituent undergoes the bivariant reaction mentioned in the prior discussion of the solidification sequence, but the subsequent univariant reaction is such that the silver-enriched liquid decomposes to terminal solid solution nickel and a gaseous metallic component. This gaseous component would form the cavities and would then condense on the inner surfaces of the cavities on undergoing the final univariant reaction on cooling. Although these reactions are of the eutectic type, they are sufficiently uncommon to be thus far unnamed. We may see, then, that these cavities could have been formed naturally, even during the solidification sequence, and because of this they were further studied.

Surface analysis of the inner surfaces of the cavities indicated that the overall surface content was well in excess of 90 percent silver and that the silver array was not simply a homogeneous silver evaporative deposit but was localized in a morphological array that was locally varied and reminiscent of the morphology of

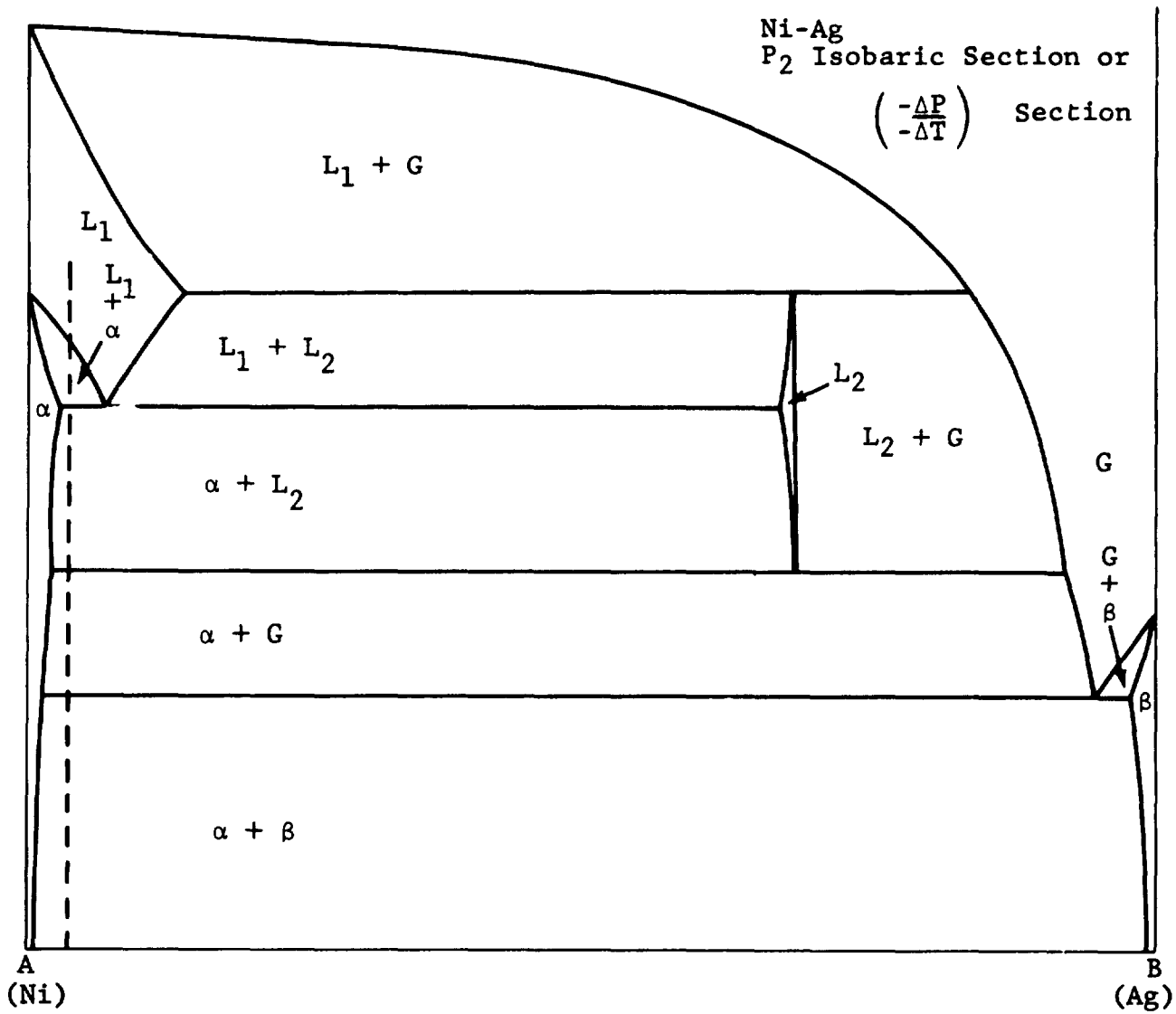

Fig. 40 Derived Phase Diagram for Ni-Ag

eutectic-type phase reactions. Two morphologies of this type in sample 1-2 are shown in Figs. 41 and 42. In these cases, the silver-rich (> 90 percent) phase appears lighter and the nickel-rich (> 90 percent) phase appears darker. More work is needed to singularly define the phase reactions in each of these regions.

An additional feature of the cavities was that the gaseous evolution had laid bare what had been the advancing solid/liquid interface. This gave some surprising results. Perhaps this would be an effective way of revealing the solid/liquid interfaces in the study of solidification mechanics and because of its natural occurrence, might minimize the last liquid effects. Clearly, this is conjecture at this point, but as previously mentioned, there was an excellent record of platelet, cellular, and dendritic growth revealed by these cavities.

Additional artifacts of interest that were revealed by these cavities are shown in Figs. 43 and 44. Figure 43 is a melting artifact and shows an unmelted dendrite, with secondary arms, that was laid bare when the surrounding liquid evaporated. This occurred because the starting Ni-1Ag alloy material was banded and in this case the solute-poor dendrite remained unmelted even as the solute-enriched layer adjacent was liquified and evaporated. Figure 44 is in a region that appeared to have been fully molten at one time and, therefore, must be considered a solidification artifact. As such, it is a highly unusual configuration and should be further considered with respect to the theoretical geometrical stability of solid/liquid interfaces.

These samples, too, had some surface regions with high levels of aluminum contamination from the pedestal. The surface analyses shown in Table 6 reflect this.

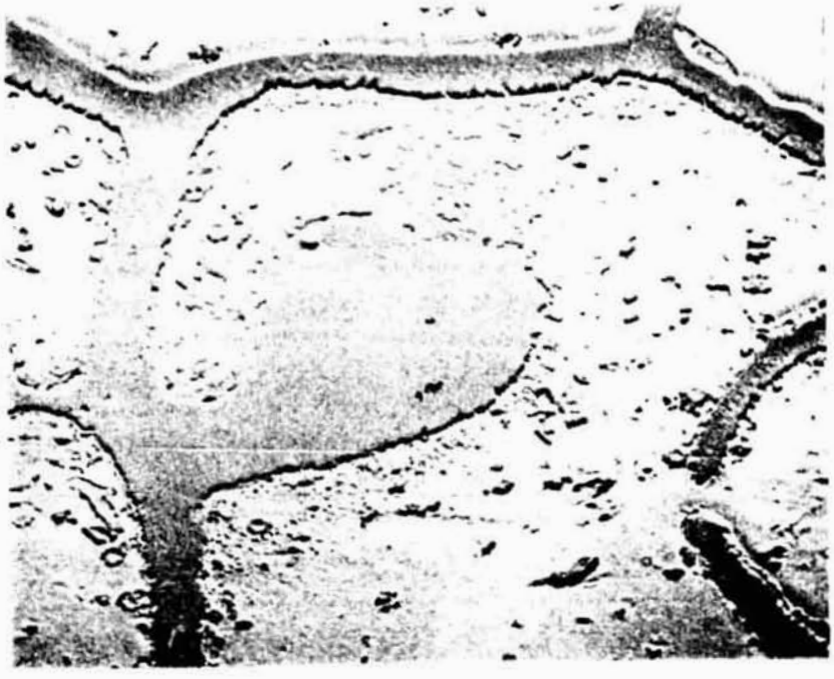

Fig. 41 Morphology of Inner Surface of Cavity, Sample 1-13, Ni-1Ag (1400×)

Fig. 42 Morphology of Inner Surface of Cavity, Sample 1-13, Ni-1Ag (1400×)

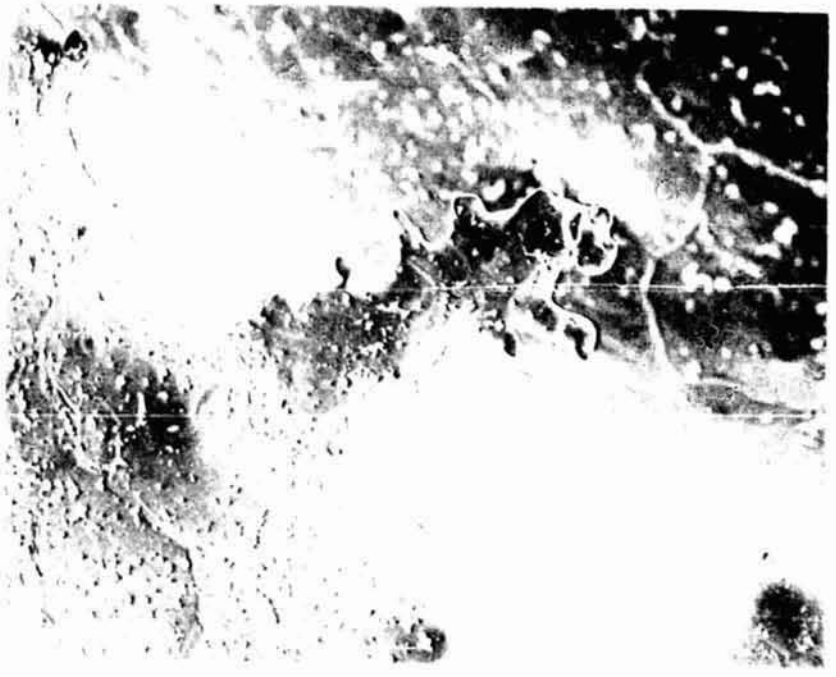

Fig. 43 Unmelted Dendrite, Sample 1-13, Ni-1Ag (350x)

Fig. 44 Solidification Artifact, Sample 1-13, Ni-1Ag (1500x)

The surface grain size of the Ni-1Ag alloy, in a region of equiaxed dendrites, was 0.20 mm whereas the surface grain size of the flight samples in equiaxed regions was 0.09 ± 0.03 mm. This is not a phenomenal difference; however, the change in the mode of solidification was altered appreciably, as previously discussed.

Because of the possibility of oxidizing the cavity surfaces and thus ruining an invaluable record of the gas/liquid/solid reactions, no Curie point measurements were run on these samples.

Lattice parameter results for the ground base sample indicated an a_o of 3.5278Å. Parameters of the flight samples were 3.52969 for sample 1-2 and 3.53017 for sample 1-13. Because of the uneven shape of these samples, however, the error in the latter measurements is appreciably higher than for the ground base sample.

In summary, we may say that the reduction of the hydrostatic pressure head (P_h), which is equal to ρgh (ρ = density, g = gravity, h = hydrostatic head) is both fundamental and significant. These samples demonstrated this effect of the reduced gravity environment and future work should quantify it analytically and apply it experimentally.

CONCLUSIONS

We may conclude that this experimentation was a substantial success even though the goal of studying containerless solidification was not reached for the majority of the samples.

We have demonstrated that the results gleaned are somewhat directly related to the sophistication, thoroughness, and resolution of the diagnostic analysis and this result should be borne in mind in planning future experimentation.

The localization of the solute rejection process, at times to specific low-index crystallographic systems, is a somewhat surprising result and should be further pursued in subsequent analysis of these samples. That corresponding localization was not found in the ground base samples is also worthy of note, and may be related to the level of convection.

The microchemical mapping of the high alloy content materials points to the importance of the thermal variables G and R, and by projection, the importance of controlling these parameters in future experimentation. Detailed mapping, from the surface inward, is required to differentiate evaporative segregation from initial transients and the various possibilities inherent to the latter consideration. This is of importance as the presumption of reduced convection in the weightless environment should manifest itself in variations of the initial transient & diffusional considerations become relatively more important.

Our analysis has defined a first order reduced gravity effect — the reduction of the hydrostatic pressure head within a liquid column or droplet. This result is unprecedented in that it offers the opportunity to exploit a range of uncommon phase reactions involving gaseous metallic phases over an extensive series of metallic

systems. This work, for most of these systems, could not be simulated terrestrially because of the pressure head. These gaseous reactions are benefited further by the reduced gravity environment in that the gas does not have a tendency to evolve because of gravitational segregation of the phases. This might be considered a second order effect of the reduced gravity environment.

Lastly, our recommendations are such that the detailed analysis of these samples should be continued, and the quantization, anticipation, and application of the pressure head reduction should be expanded. These samples effectively broaden the scope of investigation from solid/liquid phenomena to solid/liquid/gas phenomena, and may indicate that space processing experiments should be planned on the basis of pressure/temperature/composition diagrams or pressure/temperature projections rather than the terrestrially standardized temperature/composition diagram.

REFERENCES

1. Tiller, W. A., Journal of Metals 9, p. 847, 1957.

2. Hansen, M., Constitution of Binary Alloys, McGraw-Hill Book Company, 1958.

3. Larson, D. J., Jr. and Li, C. H., Monthly Progress Report No. 3, Contract NAS 8-28728 (included as Appendix B).

4. Larson, D. J., Jr., "Investigation of Ground Base Simulation Skylab Samples," Grumman Research Department Memorandum RM-576, August 1973.

5. Chalmers, B., Principles of Solidification, John Wiley & Sons. Inc., 1964.

6. Drazin, M. P. and Ott, H. M., Tables for Determining Cubic Crystal Orientations from Surface Traces of Octahedral Planes, The Paul M. Harrod Co., Baltimore, Marylan..

APPENDIX A

PHASE DIAGRAMS

Since the phase diagrams (Hansen, Ref. 2) for the three binary alloys used in the M553 experiment are referred to so extensively in this report we reproduce them here. They comprise this appendix as follows:

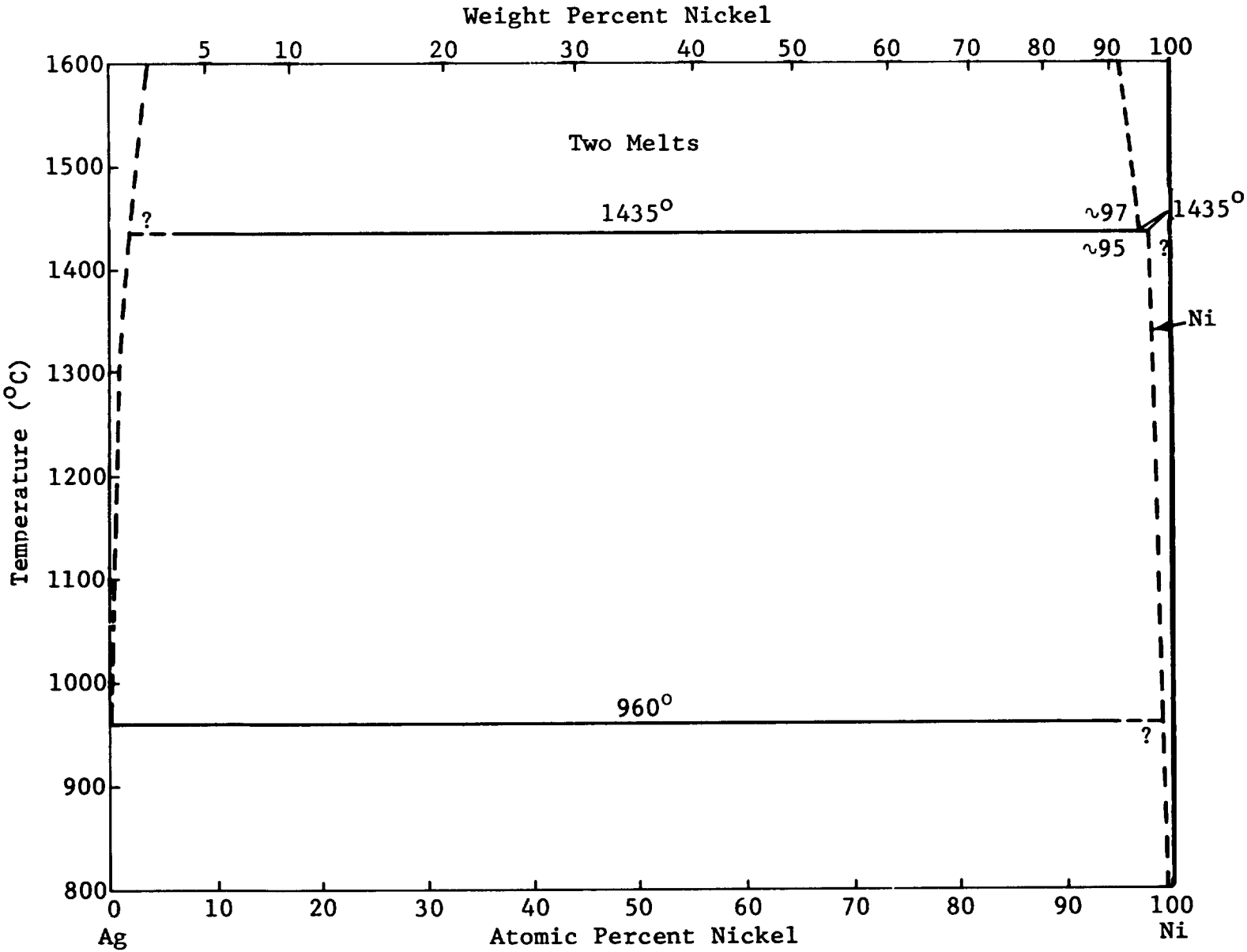
Weight Percent Nickel
5
10
20
30
40
50
60
70
80
90
100
1600
1500
1400
1300
1200
1100
1000
900
800
Temperature (°C)
Two Melts
1435°
?
~97
~95
1435°
?
Ni
960°
?
0
10
20
30
40
50
60
70
80
90
100
Ag
Atomic Percent Nickel
Ni

Fig. A-1

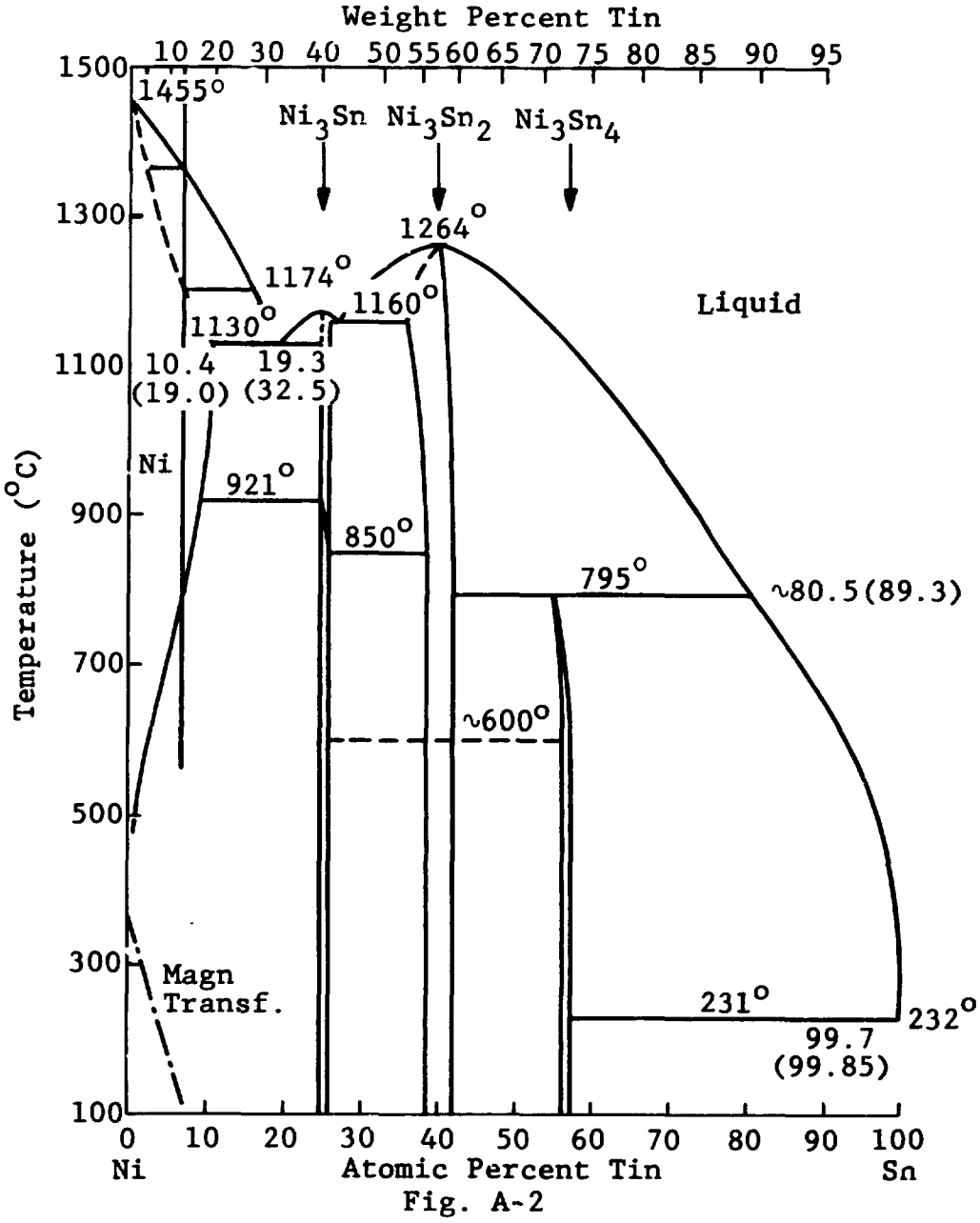
Weight Percent Tin
10 20 30 40 50 55 60 65 70 75 80 85 90 95
1500
1300
1100
900
700
500
300
100
Temperature (°C)
1455°
Ni3Sn
Ni3Sn2
Ni3Sn4
1264°
1174°
1160°
1130°
Liquid
10.4
(19.0)
19.3
(32.5)
Ni
921°
850°
795°
~80.5(89.3)
~600°
Magn
Transf.
231°
232°
99.7
(99.85)
0 10 20 30 40 50 60 70 80 90 100
Ni
Atomic Percent Tin
Sn

Fig. A-2

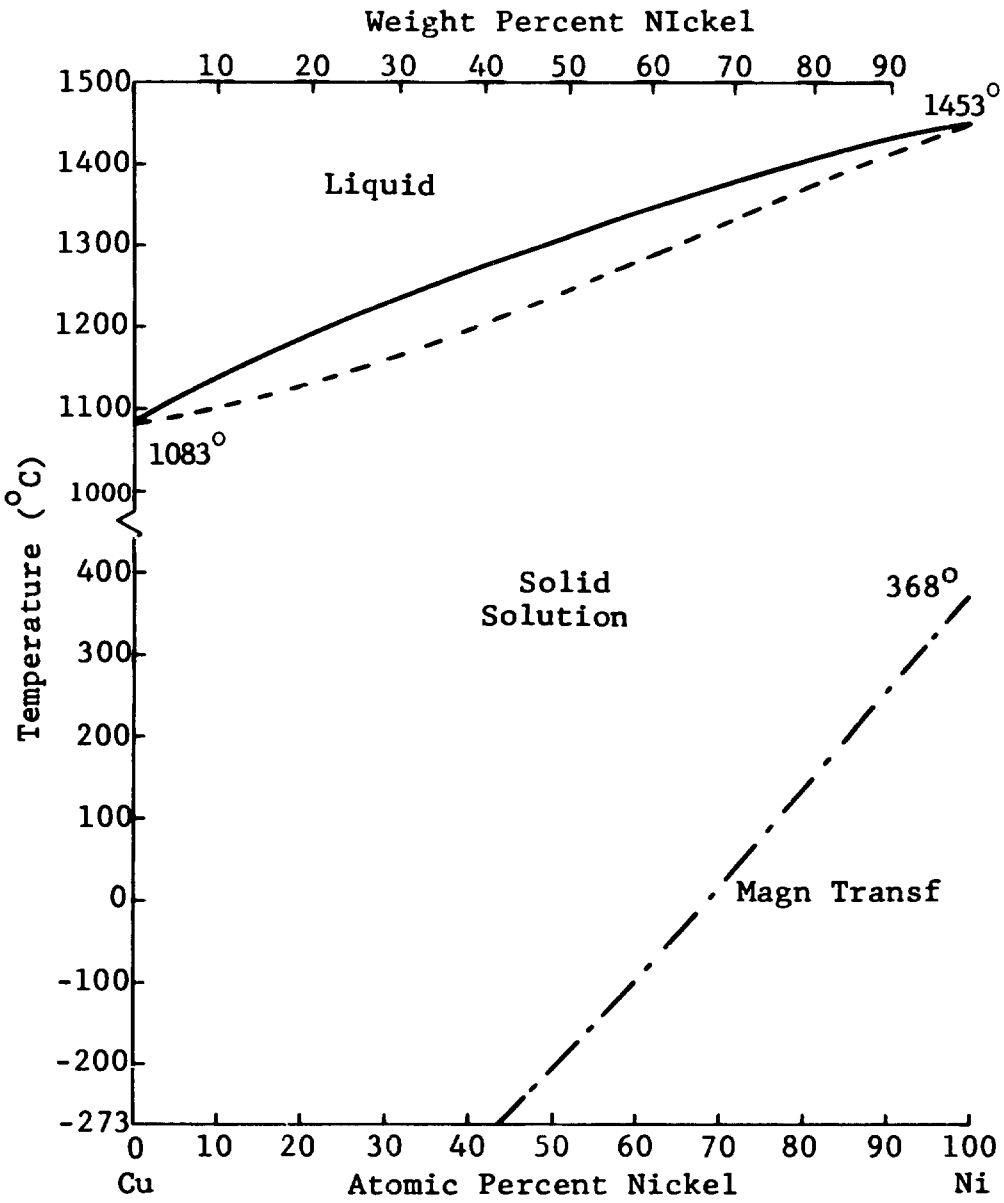
Weight Percent NIckel
10 20 30 40 50 60 70 80 90
1500
1400
1300
1200
1100
1000
400
300
200
100
0
-100
-200
-273
1453°
Liquid
1083°
Solid
Solution
368°
Magn Transf
Temperature (°C)
0 10 20 30 40 50 60 70 80 90 100
Cu
Atomic Percent Nickel
Ni

Fig. A-3

APPENDIX B

STUDY ON MATERIALS PROCESSING IN SPACE EXPERIMENT M512

The information generated on the ground base specimens has been included in this appendix; it was originally presented in Progress Statement No. 3. Because of the limited distribution of this Statement, we felt it worth while to reproduce it in this appendix. The Progress Statement follows.

The final materials for the M553 sphere forming experiment of the M512 Materials Processing in Space Program are as follows:

1. Pure nickel
2. Ni-1 wt % Ag (Ni-0.55 at. % Ag)
3. Ni-12 wt % Sn (Ni-6.32 at. % Sn)
4. Ni-30 wt % Cu (Ni-28.6 at. % Cu)

Experiments were previously performed on the Ni-5 wt % Al (Ni-10.28 at. % Al) alloy and the Star-J Stellite. The data on the Ni-5 wt % Al are included in this appendix.
As we had no Ni-30 wt % Cu available to us, we utilized K-Monel, which is nominally 66 Ni-30 Cu-3 Al (wt %) and that should demonstrate physical characteristics similar to Ni-30 wt % Cu. As a result of this "approximation," the deviations inherent in this system are greater than for the carefully prepared materials that are representative of flight materials.

Our work for the past month has consisted of designing a recommended Skylab experiment specimen test sequence, which is included as Table B-1, and in laboratory work on both the KC-135 flight samples and the as-received Skylab materials, or reasonable facsimiles. The KC-135 data will be presented in complete form in a separate report since the electron microproble and scanning electron microscopy results are not yet completed. Our work has included melting point studies, metallography, X-ray diffraction, hardness, and Curie point measurements. Our analysis has been conducted on the basis that these alloys are all essentially single phase isostructural, nickel solid solutions.

Designed Experiment

A statistically designed experiment for maximum scientific return has been set up for the M553 experiment. This experimental plan, given in Table B-1, specifically designates the arrangement of the 30 samples on the two cartwheels. The logic of the design is as follows: There are two wheels each having 15 positions to accommodate 15 samples. Position No. 1 on each wheel is reserved for

TABLE B-1

M553 SPECIMEN SEQUENCE

POSITION	WHEEL NO. 1	WHEEL NO. 2
	Retained Samples	
1	W	W
2	Ni	Ni-Cu
3	Ni-Sn	Ni-Ag
4	Ni-Cu	Ni-Sn
	Detached Samples	
5	Ni	Ni
6	Ni-Sn	Ni-Sn
7	Ni-Ag	Ni-Ag
8	Ni-Cu	Ni-Cu
9	Ni-Cu	Ni-Cu
10	Ni-Ag	Ni-Ag
11	Ni-Sn	Ni-Sn
12	Ni	Ni
13	Ni-Cu	Ni
14	Ni-Ag	Ni-Sn
15	Ni-Sn	Ni-Ag

Electron beam heating parameters to be assigned later for each specimen.

tungsten samples, used to align the electron beam. In addition, three samples (at Positions 2-4) on each wheel are to be melted without releasing, to study the effect of zero-gravity melting and constrained solidification. This leaves 11 positions on each wheel for the actual experiment on zero-gravity melting and free solidification.

Altogether, four sample materials are to be tested — pure Ni, Ni-Ag, Ni-Sn, and Ni-Cu. On Positions 2 to 4 of Wheel 1, the samples are arranged in the order of pure Ni, relatively low-evaporating Ni-Sn, and Ni-Cu. The order was, therefore, set up to minimize contamination from previously melted samples. Positions 2 to 4 of Wheel 2 are for Ni-Cu, Ni-Ag, and Ni-Sn, respectively. The purpose of this arrangement is threefold: to cover the remaining Ni-Ag sample not tested on Wheel 1, to give some idea about contamination (i.e., Cu on Ag and Ag on Sn), and to give duplicated test results on melted but unreleased Ni-Sn and Ni-Cu samples.

Positions 5-12 on the wheels form the "body" of the designed experiment. The sequencing arrangements are identically the same on both wheels, to give substantive duplicated results. It is noted that the sequencing for Positions 9-12 is the mirror image of that for Positions 5-8. This is to obtain information not only on the experimental error within each wheel, for comparison between wheels, but also information on the possibly important or even dominating "time" effect. As was pointed out in the M553 review meetings, the vacuum in the test chamber generally deteriorates, the astronauts become fatigued, the Skylab orbiting (and 0-g) conditions change, ..., with heating and melting of each additional sample. Our design allows us to estimate this time effect, be it large or small.

The electron beam heating parameters (e.g., beam current or focusing conditions) may also be studied on the same wheels and samples, if their sequences are properly superimposed onto the design (Table B-1). Even if the samples are to be tested in 2 or 4 (not 3 or 5!) laboratories, the same design can be similarly supplemented so that the effect of laboratory-to-laboratory variations, and/or electron beam heating parameters, can be qualitatively identified and quantitatively estimated.

Samples on Positions 13-15 are dummies or spares, in case of accidents to the samples on Positions 2 to 12. These last six samples are additionally useful in giving an accurate estimate of the experimental error connected with each wheel. This error allows us to evaluate the statistical significance of the various material, time, heating, and laboratory parameters.

The sequencing in Table B-1 is very carefully arranged for perfect balance, so that each of these effects is orthogonal relative to any other (i.e., there is no mixing of effects) but can be independently and accurately estimated. Any random switch in the sample positions is likely to disturb this delicate balance and make the experiment much less efficient, if not altogether destroying the capability of the resulting data being analyzed meaningfully.

X-Ray Diffraction

X-ray diffraction confirmed that each alloy investigated is face-centered cubic nickel solid solution, with almost no second phase particles. The second phase particles, if present, will be analyzed for the one-g samples processed from a received Skylab flight material, but no effort was expended in this regard for

these facsimile materials. The experimental and theoretical lattice parameters for nickel and the four nickel alloys are presented in Table B-2. The theoretical values were calculated utilizing the

TABLE B-2

EXPERIMENTAL AND THEORETICAL LATTICE PARAMETERS FOR SKYLAB MATERIALS

ALLOY	LATTICE PARAMETERS (A) (THEORETICAL)	(EXPERIMENTAL)
Ni	3.5355	3.534 ± .001
Ni-1Ag	3.5385	3.533 ± .001
Ni-12Sn	3.5945	3.593 ± .005
Ni-5Al	3.5879	3.542 ± .002
K-Monel *	3.5625	3.581 ± .004
Ni-30Cu	3.5625	3.5325 ± .0006 (3)

* K-Monel - Ni-30Cu-3Al

assumption of ideal mixing with no electronegative interaction and Goldschmidt radii of 1.25, 1.28, 1.43, 1.44, and 1.58 for Ni, Cu, Al, Ag, and Sn, respectively (Ref. B-1). These values have been corrected to twelvefold coordination in each case. Of course, this Vegard-type mixing is only an approximation, and is not strictly appropriate for metallic solid solutions, but it is a basis for initial comparison.

It is clear that in general the experimental trend closely follows the sequence of calculated lattice parameters, although the K-Monel evidences a positive deviation and the Ni-5Al a negative deviation from the theoretical value. The latter deviation is likely to be electronegative in nature although there is the distinct possibility that this casting is significantly deficient

in aluminum. This point will be resol ed by chemical analysis within the next month. Actually, on the basis of the electron volume theory for solid solutions (Ref. B-2), one would predict that the experimental lattice parameters for Ni-Ag and Ni-Cu alloys would be smaller than the theoretical value, whereas the Ni-Al and Ni-Sn experimental lattice parameters would be slightly larger, neglecting electronegativity effects. As is seen, the Ni-Ag and Ni-Sn alloys agree with this, the Ni-Al alloy (if the chemistry is correct) evidences a contraction due to electronegativity, and the K-Monel will be discounted until a true binary Ni-30 Cu alloy is available for analysis. The published lattice parameters for a Ni-30 Cu alloy evidence the anticipated negative deviation from the theoretical value (Ref. B-3).

Hardness

Hardness is dependent on alloy composition and the thermomechanical state of the sample at the time of the hardness test. Just as mechanical work (strain) can result in a hardness increase, so can lattice strain. This is the basis for solid solution hardening. Consequently, materials to be compared on the basis of hardness should have the same thermomechanical history. Our samples do not. It is still possible, however, to make some sense of the respective hardness values that are presented in Table B-3 and in Fig. 1. As

TABLE B-3

ALLOY HARDNESS (D.P.H.)

ALLOY	HARDNESS	TICE STRAIN	DESCRIPTOR
Ni	90	0	Annealed
Ni	275	--	Wrought
Ni-1Ag	72	-.017 to -.04	As Cast
Ni-12Sn	290	+1.53 to 1.81	Recrystallized
Ni-5Al	123	+.7 to .28	As Cast
K-Monel	140-180	+.2 to 1.45	Wrought and Annealed

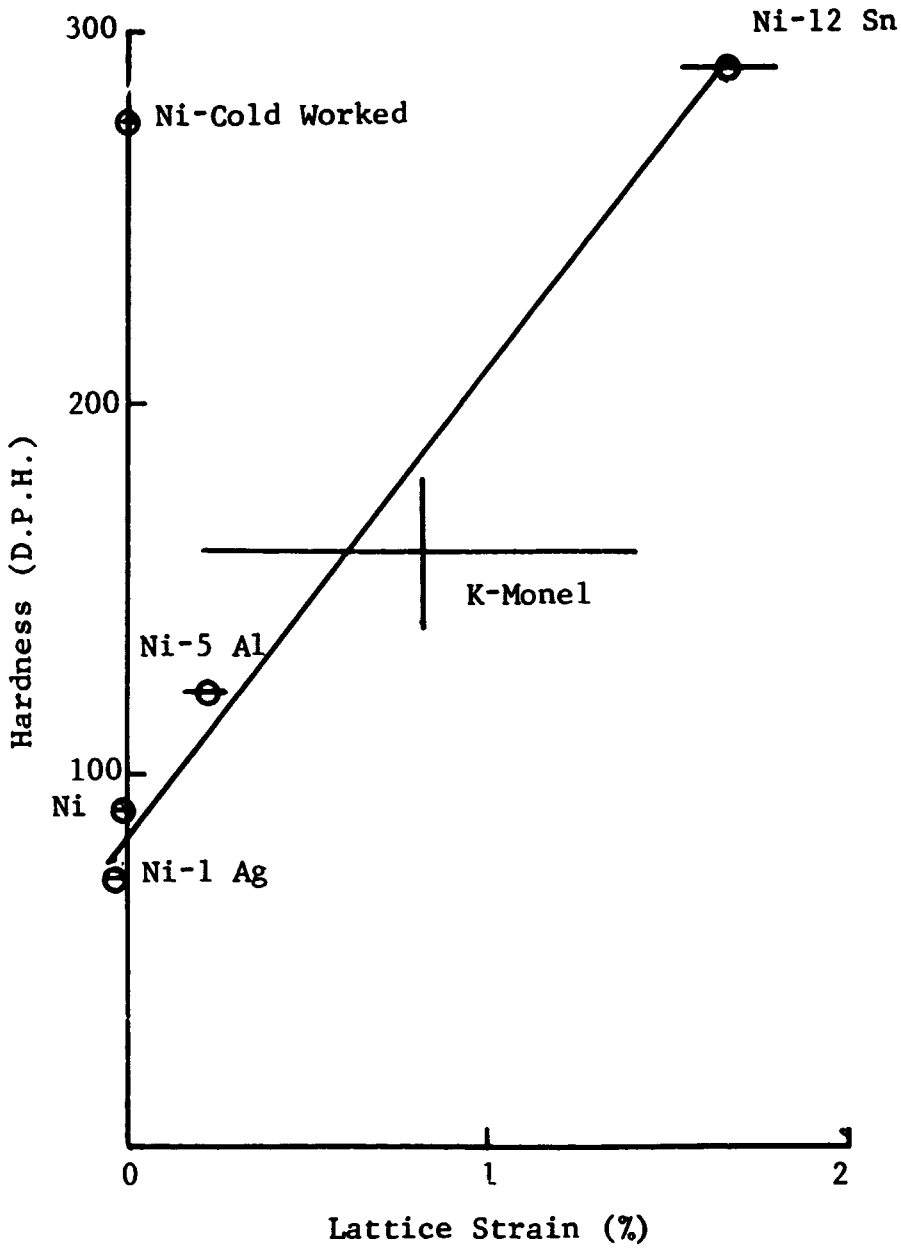

Fig. B-1 Hardness versus Lattice Strain

is seen in Fig. B-1, the hardness associated with the respective solid solutions is linearly related to the experimentally measured lattice strain introduced by the alloying. This is to be anticipated. The significance of mechanical strain is shown by the single wrought nickel (worked) data point for pure nickel, and probably by the hardness range associated with the K-Monel. This correlation of lattice strain to sample hardness should be pursued within the group of flight samples, with careful regard for the masking effects of mechanical work.

Microstructure

The microstructure of the respective alloys is shown in Figs. B-2 through B-6 and the differences in microstructure are readily apparent. The pure (wrought) nickel microstructure (Fig. B-2) shows that this as-received material has not completely recovered from the mechanical work of forming. Also shown is an arm of the centerline crack that was found in some regions of the as-received nickel rod. The Ni-12 Sn rod was apparently recrystallized; however, it has an average grain size of 50 micrometers and that is significantly smaller than that of an as-cast or fully-annealed microstructure (Fig. B-3). The K-Monel sample evidenced a mixed microstructure that was composed of a few large grains intermixed in a "matrix" of small, equiaxed grains (Fig. B-4). The as-cast Ni-1 Ag microstructure demonstrates a moderate grain size with both wide, high angle boundaries and decorated, low angle boundaries. There are extremely fine homogeneous, precipitate particles, but these comprise only a small proportion of the sample volume. This is shown in Fig. B-5. The as-cast Ni-5 Al microstructure (Fig. B-6) exhibits an extremely large grain size and narrow, high angle, grain boundaries. This sample also demonstrates extensive prismatic slip under the hardness indentor, as shown in Fig. B-6.

Melting Point Studies

These studies were conducted in a DuPont 900 differential thermal analyzer (DTA) under an atmosphere of argon or a flux of SiO_2. The results of each technique were similar with the exception of the Star-J, as this cobalt base alloy reacted with the flux. As a result, subsequent Star-J studies were all carried out in an argon atmosphere. The results of this study are tabulated in Table B-4. These data are intended only to determine the liquidus and solidus temperatures, and subsequent work, outlined

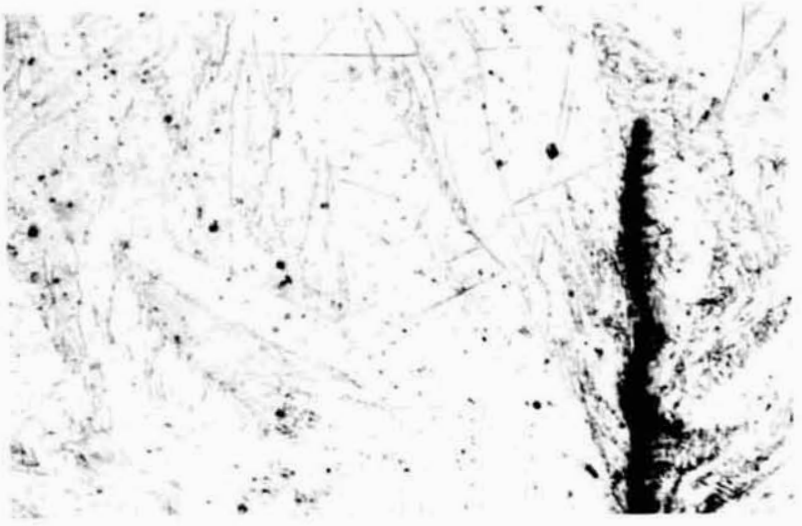

Fig. B-2 Microstructure of Wrought Nickel Rod (150x)

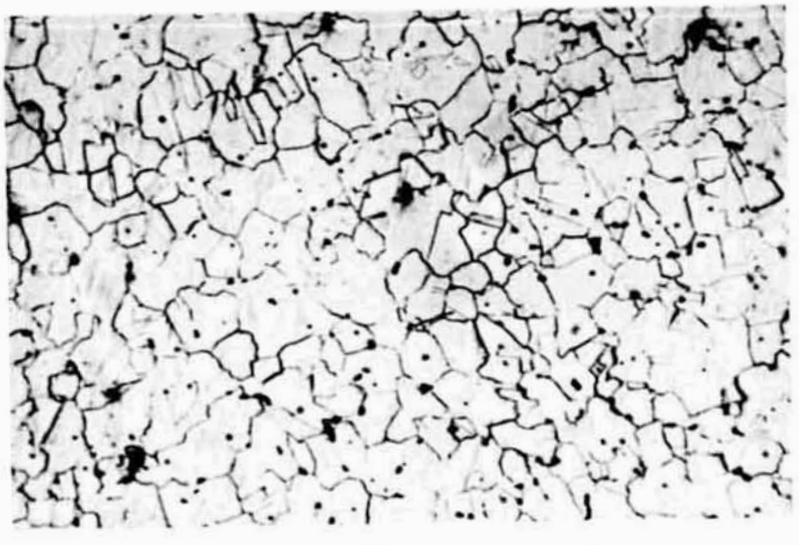

Fig. B-3 Microstructure of Wrought Ni-12 Sn Rod (150x)

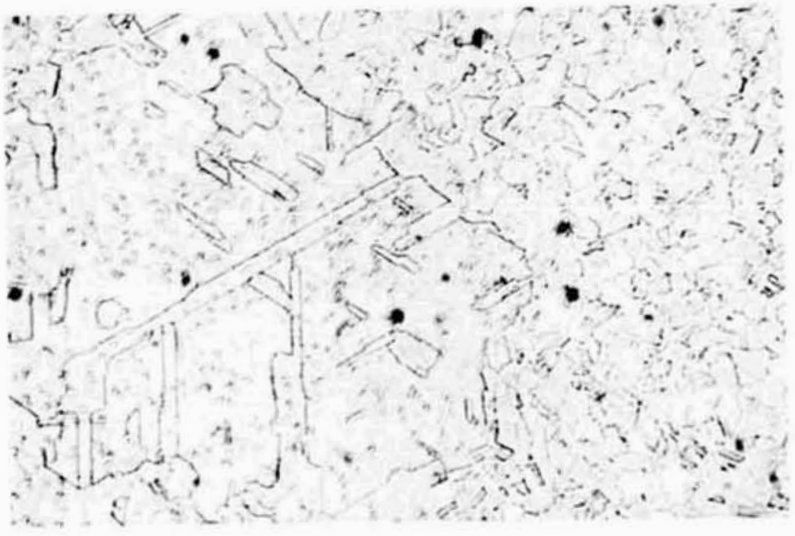

Fig. B-4 Microstructure of Wrought K-Monel Rod (150x)

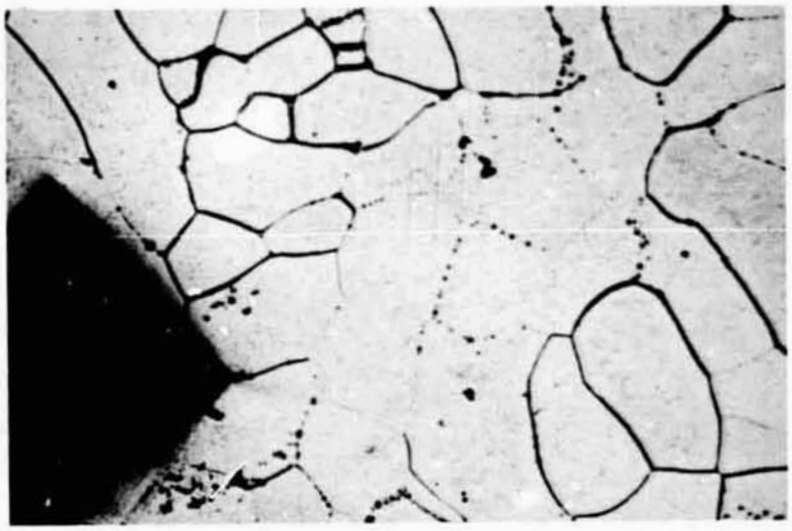

Fig. B-5 Microstructure of As-Cast Ni-1 Ag Alloy (150x)

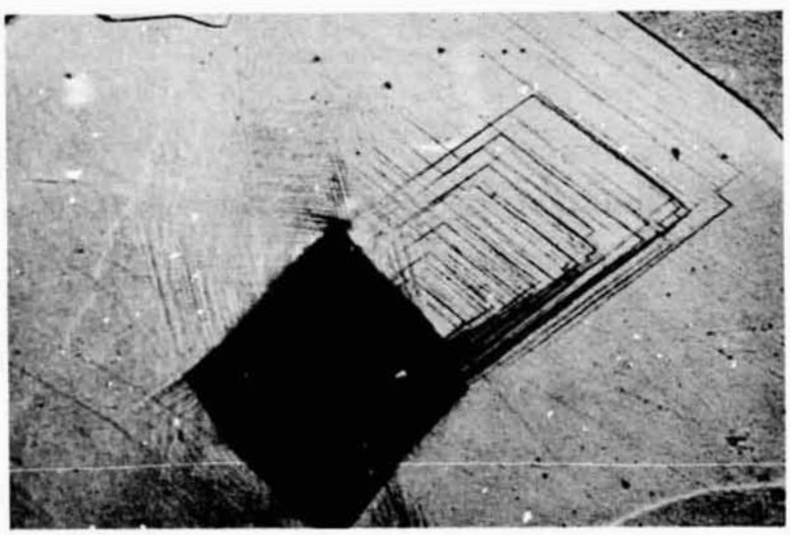

Fig. B-6 Microstructure of As-Cast Ni-5 Al Alloy (150x)

TABLE B-4

MELTING POINTS STUDIES

ALLOY	HEATING RATE	LIQUIDUS	SOLIDUS	T MEAN
Ni-5Al	10°C/Min	1502°C	1442°C	1472°C
	1°C/Min	1481°C	1466°C	1473.5°C
Ni-1Ag	10°C/Min	1475°C	1405°C	1440°C
Ni-12Sn	10°C/Min	1372.5°C	1268°C	1320°C
Star-J	10°C/Min	1280°C	----	----
Nickel	10°C/Min	1462°C	1446°C	1454°C
K Monel	10°C/Min	1350°C	1310°C	1330°C

in our Phase B Study Plan, will determine the effects of varying heating rates, cooling rates, degree of superheat on the structure and degree of undercooling on the actual flight materials.

Curie Point Studies

These studies were conducted in air in a DuPont 900 differential scanning calorimeter (DSC) and the intent was to determine the effect of alloying on the magnetic properties of the nickel solid solution.

Nickel has 10 (3d + 4s) electrons that are thought to fill the overlapping d and s bands in such a way that one of the half bands of the 3d state is completely full and the other lacks 0.6 of an electron per atom of being filled (Ref. B-1). When a solute atom is substituted for an atom of nickel in the solid solution, electrons are substituted for the original 10 (3d + 4s) electrons. If we consider a copper addition, 11 (3d + 4s) electrons are substituted for the original 10; i.e., the solid solution has gained an extra electron by this substitution. This extra electron must go into the partially empty half band, filling it slightly, and

consequently reducing the net magnetization. This decrease in net magnetization will also manifest itself in a lowered magnetic transformation temperature so that less thermal motion of the atoms is required to misalign the spins. The addition of monovalent copper does result in the predicted Curie point decrease in temperature and it would also be anticipated that the addition of monovalent silver would act similarly. Trivalent aluminum would act even more rapidly, and tetravalent tin would suppress the Curie point most rapidly. This is found to occur, as tabulated in Table B-5 and

TABLE B-5

CURIE POINTS FOR THE SKYLAB ALLOYS

ALLOY (a.%)	VALENCE	CURIE POINT (C°)	CURIE POINT SUPPRESSION(Δ T) PER a.% ADDITIVE (°C/a. %)
Ni	2	358	----
Ni-.55Ag	1	351	12.70
Ni-28.6Cu	1	58	10.49
Ni-10.28Al	3	139	22.37
Ni-6.32Sn	4	105	40.03
K Monel	1.3	-90	----
Star- J	---	<-196	----

plotted in Fig. B-7. Although the decrease in the Curie point is very close to being directly proportional to the valence of the alloying element, for these solid solutions, it is not felt that a simple direct correlation should be immediately inferred. These data points are calculated on the basis of the first significant deviation from the sample baseline. It should be noted that the temperatures of the completion were not as consistent with theory, nor were they as well defined.

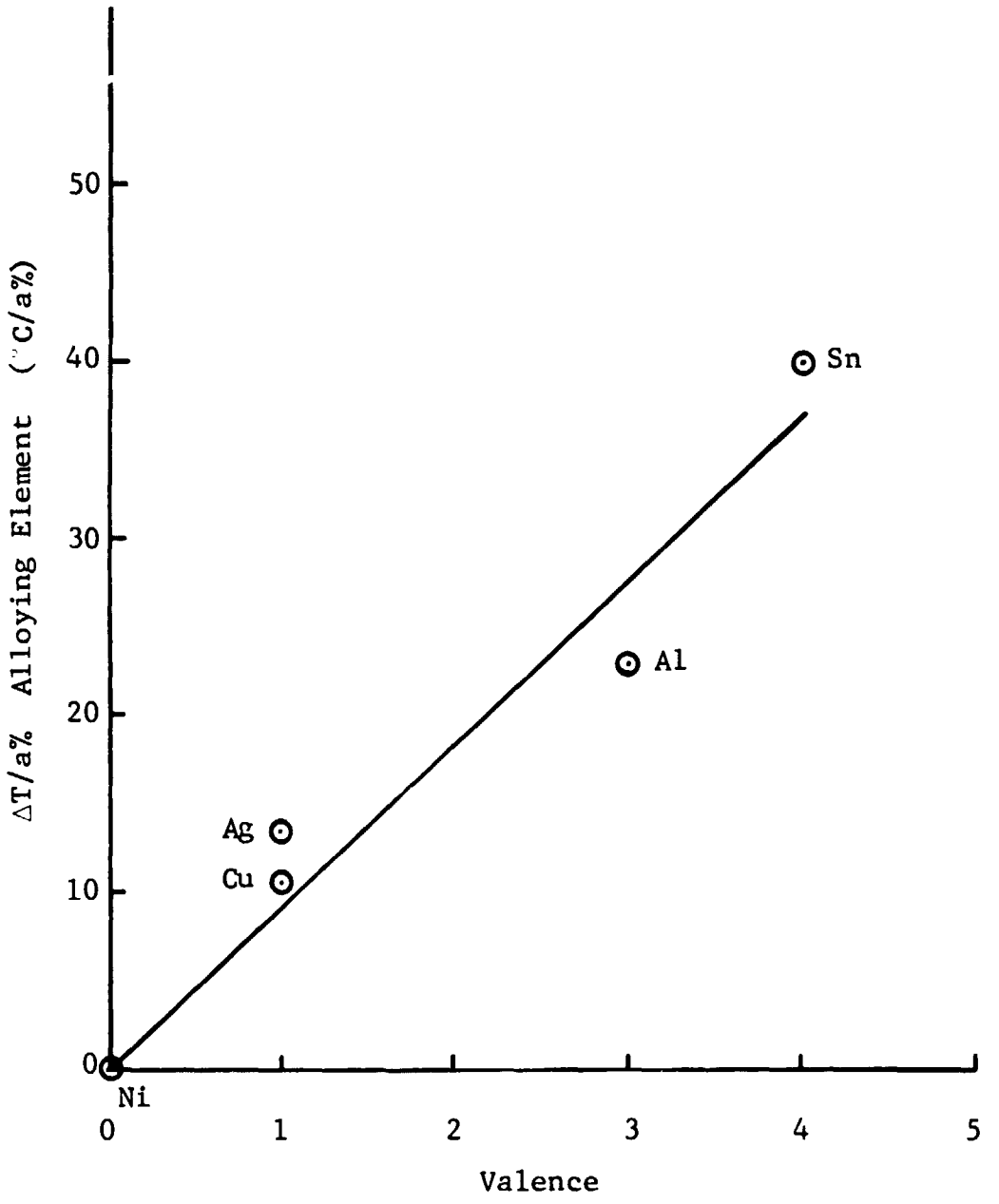

Fig. B-7 Curie Point Suppression versus Valence of Alloying Element

References

B-1. Wert, C. and Thomson, R., Physics of Solids, McGraw-Hill Book Company, 1964.

B-2. Hume-Rothery. W. and Raynor, G., The Structure of Metals and Alloys, Institute of Metals, 1962.

B-3. Coles, B., J. Institute of Metals, Vol. 84, 1956, p. 346.